An Evaluation of the FCT Method for High-Speed Flows on Structured Overlapping Grids

J.W. Banks [1,2], and W.D. Henshaw [1]

Center for Applied Scientific Computing, Lawrence Livermore National Laboratory,
Livermore, California , 94551

J.N. Shadid [2],

Computational Sciences R&D Group, Sandia National Laboratories,
Albuquerque, New Mexico, 87185-1322

Abstract

This study focuses on the development and assessment of a Flux-Corrected Transport(FCT) algorithm for simulating high-speed flows on structured overlapping meshes. This class of algorithm shows promise for solving some difficult highly-nonlinear problems where robustness and control of certain features, such as maintaining positive densities, is important. Complex, possibly moving, geometry is treated through the use of structured overlapping meshes and adaptive mesh refinement (AMR) is employed to ensure sharp resolution of discontinuities in an efficient manner. Improvements to the FCT algorithm are proposed for the treatment of strong rarefaction waves as well as rarefaction waves containing a sonic point. The order-of-accuracy of the FCT method is demonstrated through convergence studies for smooth manufactured solutions. Simulation results are obtained for a set of test problems and the convergence characteristics of the method demonstrated. Comparison to a high-resolution Godunov method provides more details concerning the performance of FCT for overlapping mehes. The set of problems considered here includes an isolated shock, an isolated contact, a modified Sod shock tube problem, a two shock Riemann problem, the Shu-Osher test problem, shock impingement on single cylinder, and irregular Mach reflection of a strong shock striking an incline plane.

Key words: Euler Equations, Flux Corrected Transport, High Resolution Methods, Overlapping Grids

1   Introduction

Many physical systems are well described mathematically by systems of conservation laws. Typical examples might include fluid flow around a body, condensed phase explosives, astrophysical phenomenon, or high energy density physics applications. A large number of such systems have the property that discontinuous solutions can arise in finite time even from smooth initial data. These discontinuities can be of a linear (e.g. contact wave) or nonlinear form (e.g. shock wave). Numerical methods need to balance the often competing requirements of accurately approximating these two types of discontinuities while at the same time requiring higher order accuracy in smooth regions of the solution. This balance has been one of the primary drivers behind the development of modern simulation tools. Methods striking such a balance are often referred to as high-resolution methods and they require the use of limiters (switches), that choose between a number of different numerical stencils. For some flow regimes, this type of limiting is essential to obtain a robust scheme. Many, if not most, of the high-resolution techniques have their roots in the 1970's with ideas originally developed by Boris and Book in connection with flux-corrected transport (FCT) [1–3]. In the intervening years, FCT has been applied to a wide range of challenging applications, for examples see [4–6], however the underlying mathematical developments have not been as extensive as for other modern high-resolution techniques such as WENO [7,8], ENO [9–11], and high-resolution Godunov techniques [12–14]. Recently however, the developments of Kuzmin et. al. [6] towards algebraic flux correction as well as implicit methods have produced a renewed interest in FCT as a useful numerical method for many applications.

The scope of our current study is in the evaluation of FCT type methods for compressible flow simulations in the context of overlapping meshes which are used to represent geometric complexities as well as ensure mesh regularity [15–18]. This type of overlapping methodology is quite general and can be used to generate computational meshes for complex geometries [19–21] without the use of unstructured meshes, cut cells for embedded boundaries, or overly contorted globally mapped meshes. The FCT method is a valuable simulation tool which has not seen use in such an infrastructure and it is the focus of this current study to evaluate its usefulness in this context.

This paper first examines implementation details for structured overlapping meshes. A series of test problems demonstrates the properties of the method for practical simulations and detailed comparison with a high-resolution Godunov method assess the relative performance of the FCT algorithm in the new broader context of overlapping meshes. Further comparison to the results presented in other works such as [22,23] gives a relatively thorough understanding of how many modern shock capturing schemes compare to one another. Such a comparison is particularly useful for cases where Riemann solution based strategies are not viable because of the complexities of the governing equations. Such is the case for some relativistic flows for example and the FCT method may be attractive in this context assuming that an appropriate low order method can be devised without resort to Riemann solutions. Furthermore, the FCT method has applicability to unstructured meshes and finite element discretizations and so understanding its performance in relation to other methods becomes important.

The remainder of the paper is structured as follows. In Section 2 the inviscid Euler equations are reviewed as the governing conservation law system. In Section 3 the FCT algorithm is presented and the development for structured overlapping meshes is summarized. This section also presents a brief discussion of two open issues with the traditional FCT algorithm; that of performance when either strong or sonic rarefactions are present in the flow. The poor performance of the standard method for these problems is demonstrated and an improvement of the algorithm is proposed and evaluated. Section 4 presents numerical results for the FCT method as well as provides a comparison to a high-resolution Godunov method. Some qualitative remarks concerning computational cost comparisons between the FCT and Godunoc methods are given in Section 5 and concluding remarks are given in Section 6.

2   Governing Equations

In this paper we consider the flow of an inviscid compressible gas and assume that in two dimensions the density ρ, velocities (u_1, u_2), pressure p, and total energy E satisfy the system of conservation laws

$$\frac{\partial}{\partial t}\mathbf{u} + \frac{\partial}{\partial x_1}\mathbf{f}_1(\mathbf{u}) + \frac{\partial}{\partial x_2}\mathbf{f}_2(\mathbf{u}) = 0, \tag{1}$$

where

$$\mathbf{u} = \begin{bmatrix} \rho \\ \rho u_1 \\ \rho u_2 \\ E \end{bmatrix} \qquad \mathbf{f}_1(\mathbf{u}) = \begin{bmatrix} \rho u_1 \\ \rho u_1{}^2 + p \\ \rho u_1 u_2 \\ u_1(E + p) \end{bmatrix} \qquad \mathbf{f}_2(\mathbf{u}) = \begin{bmatrix} \rho u_2 \\ \rho u_1 u_2 \\ \rho u_2{}^2 + p \\ u_2(E + p) \end{bmatrix}.$$

System (1) defines the conservation of mass, momenta, and total energy for the gas and is recognized as the well known compressible Euler equations in two space dimensions. In this formulation, the total energy is given by

$$E = \rho e + \frac{1}{2}\rho\left(u_1{}^2 + u_2{}^2\right),$$

where $e = e(\rho, p)$ is the specific internal energy, which is specified by an equation of state (EOS). This equation of state could have a very general form but in the interest of clarity, this paper assumes an ideal equation of state, namely

$$e = \frac{p}{\rho\,(\gamma - 1)} \tag{2}$$

where $\gamma = \frac{c_p}{c_v}$ is the ratio of (constant) specific heats with c_p the specific heat at constant pressure and c_v the specific heat at constant volume. The Euler equations (1) are assumed to have been non-dimensionalized with suitable reference quantities and all results are presented in dimensionless units.

3   Flux-Corrected-Transport Algorithm

This section describes the FCT method as used in this paper including any extensions and modifications we have made to the classic FCT algorithm. This implementation include the inclusion of a DeVore type pre-limiter in lieu of Zalesak's flux pre-constraint, removal of artificial diffusion prior to the FCT flux limiter, inclusion of a Jameson style artificial viscosity, inclusion of a sonic fix for entropy violating rarefaction waves, and the extension of the FCT algorithm to overlapping grids. For clarity, the proposed improvements for treating sonic points and very strong rarefactions are left to the end of the section.

3.1   Overlapping grids and AMR

We consider the governing equations (1) and proceed with a description of the FCT method in a two dimensional overlapping grid framework. To this end, we assume the flow domain is given by Ω and that it is discretized using an overlapping grid $\mathcal{G}$. The overlapping grid consists of a set of component grids $\{\mathcal{G}_i\}$, $i = 1, \ldots, \mathcal{N}_g$, that cover Ω and overlap where they meet. Each component grid covers a domain Ω_i in physical space and is defined by a mapping from physical space (x_1, x_2) in two dimensions to the unit square (r_1, r_2) in computational space. Grid points are tagged as discretization points where the governing equations are applied, ghost points used for the application of boundary conditions, or unused points where no computation is performed which are cut out through the mesh generation procedure. The FCT stencil is 7-points wide and so three layers of ghost cells are used for this work. For more details concerning general overlapping grid methods see [15–17,24]. Adaptive mesh refinement (AMR) is used in regions of the flow where the solution changes rapidly, such as near shocks and contact surfaces. We employ a block-structured AMR approach following that described originally in [25] and using modifications for overlapping grids as presented in [16–18].

3

3.2 FCT Discretization on a mapped grid

Each component grid, including base-level grids and any refined grids, is defined by a mapping from the unit square in computational space (r_1, r_2) to physical space (x_1, x_2). In computational space, equation (1) becomes

$$\frac{\partial}{\partial t}\mathbf{u} + \frac{1}{J}\frac{\partial}{\partial r_1}\mathbf{F}_1(\mathbf{u}) + \frac{1}{J}\frac{\partial}{\partial r_2}\mathbf{F}_2(\mathbf{u}) = 0, \tag{3}$$

where

$$\mathbf{F}_1(\mathbf{u}) = J\left(\frac{\partial r_1}{\partial x_1}\mathbf{f}_1 + \frac{\partial r_1}{\partial x_2}\mathbf{f}_2\right), \qquad \mathbf{F}_2(\mathbf{u}) = J\left(\frac{\partial r_2}{\partial x_1}\mathbf{f}_1 + \frac{\partial r_2}{\partial x_2}\mathbf{f}_2\right),$$

and

$$J = \left|\frac{\partial(x_1, x_2)}{\partial(r_1, r_2)}\right|.$$

The metrics of the mapping, $\frac{\partial x_1}{\partial r_2}$, $\frac{\partial x_2}{\partial r_2}$, etc., and the Jacobian are considered to be known for each component grid at the time of computation and can be generated analytically or approximated.

Discretization of (3) is performed using a uniform grid $(r_{1,i}, r_{2,j})$ with grid spacing $(\Delta r_1, \Delta r_2)$. The FCT method is generally considered a two-step process proceeding first with a low order update and finishing with the high-resolution FCT correction. We begin with the formulation of the low order solution update

$$\mathbf{u}_{i,j}^{\text{td},n} = \mathbf{u}_{i,j}^n - \frac{\Delta t}{J_{i,j}\Delta r_1}D_{+r_1}\mathbf{F}_{1_{i-1/2,j}}^{\text{low},n} - \frac{\Delta t}{J_{i,j}\Delta r_2}D_{+r_2}\mathbf{F}_{2_{i,j-1/2}}^{\text{low},n} \tag{4}$$

where D_{+r_1} and D_{+r_2} are the undivided forward difference approximations in the r_1 and r_2 directions of index space respectively. The "td" notation is consistent with [1–3,26] and denotes "transported and diffused". For this work the HLL low order flux is used and for curvilinear geometries is given by

$$\mathbf{F}_{1_{i+1/2,j}}^{\text{low},n} = \begin{cases} \mathbf{F}_{1_{i,j}}^n & \text{if} \quad s_l \geq 0 \\ \mathbf{F}_{1_{i+1,j}}^n & \text{if} \quad s_r \leq 0 \\ \dfrac{s_+}{s_+ - s_-}\mathbf{F}_{1_{i,j}}^n - \dfrac{s_-}{s_+ - s_-}\mathbf{F}_{1_{i+1,j}}^n + \dfrac{s_- s_+}{s_+ - s_-}D_{+r_1}\mathbf{u}_{i,j}^n & \text{else} \end{cases} \tag{5}$$

where

$$s_\pm = \min\left(u_{1_{i,j}}^n \pm c_{i,j}^n, u_{i+1,j}^n \pm c_{i+1,j}^n\right)\left\|\left(\frac{\partial r_1}{\partial x_1}, \frac{\partial r_1}{\partial x_2}\right)\right\|_2,$$

and $c_{i,j}^n$ is the sound speed in a given cell. The fluxes across other cell boundaries take similar forms. Further details concerning implementation of this HLL flux can be found in [12] and [14]. It should be noted that in [27,6], Zalesak suggests the use of the Rusanov flux for the low order method. This is a symmetrized version of the HLL flux resulting in further diffusion than the original HLL flux. It is crucial to note however, that the Rusanov flux as presented in [27,6] is flawed in that the selected wave speed is not sufficient to encompass the full Riemann solution for all cases. The correct Rusanov flux is

$$\mathbf{F}_{1_{i+1/2,j}}^{\text{low},n} = \frac{1}{2}\left[\left(\mathbf{F}_{1_{i+1,j}}^n + \mathbf{F}_{1_{i,j}}^n\right) - \max\left(\left|\lambda_{i+1,j}^n\right|, \left|\lambda_{i,j}^n\right|\right)D_{+r_1}\mathbf{u}_{i,j}^n\right] \tag{6}$$

where $\lambda_{i,j}^n$ is the largest eigenvalue (in magnitude) of the Jacobian matrix $\frac{\partial}{\partial \mathbf{u}}\mathbf{F}_1$ at a cell (i, j) and time t_n. The difference between (6) and the equation presented in [27,6] is the use of $\max\left(\left|\lambda_{i+1,j}^n\right|, \left|\lambda_{i,j}^n\right|\right)$ rather than $1/2\left(\left|\lambda_{i+1,j}^n\right| + \left|\lambda_{i,j}^n\right|\right)$. The result is that when using (6), the resultant multiplier is large enough to contain the full Riemann solution and so the associated problems are avoided [14]. In this work, the HLL flux is used but we have found that the Rusanov flux (6) works nearly as well and is slightly less computationally expensive.

The second step of the FCT algorithm requires an "anti-diffusive" flux which is defined as the difference between a high order flux and the low order one

$$\mathbf{F}_{k_{i\pm 1/2,j}}^{\mathrm{AD},n} = \mathbf{F}_{k_{i\pm 1/2,j}}^{\mathrm{high},n} - \mathbf{F}_{k_{i\pm 1/2,j}}^{\mathrm{low},n} \tag{7}$$

for $k = 1, 2$. The high order flux is typically chosen to be some high-order centered flux and as far as this work is concerned the centered second order flux is chosen. The final sub-step update is now defined as

$$\mathbf{u}_{i,j}^{\mathrm{new}} = \mathbf{u}_{i,j}^{\mathrm{td},n} - \frac{\Delta t}{J_{i,j}\Delta r_1} D_{+r_1} \alpha_{i-1/2,j}^n \mathbf{F}1_{i-1/2,j}^{\mathrm{AD},n} - \frac{\Delta t}{J_{i,j}\Delta r_2} D_{+r_2} \alpha_{i,j-1/2}^n \mathbf{F}2_{i,j-1/2}^{\mathrm{AD},n} \tag{8}$$

where the vector of α's are chosen using the FCT algorithm as described below. The choice of notation facilitates the use of the FCT algorithm in a method of lines type approach. By defining

$$\frac{\partial}{\partial t}\mathbf{u}_{i,j}^n = \frac{\mathbf{u}_{i,j}^{\mathrm{new}} - \mathbf{u}_{i,j}^n}{\Delta t} \tag{9}$$

we can obtain an updated solution $\mathbf{u}_{i,j}^{n+1}$ using any ordinary differential equation (ODE) integrator we choose. Choices for ODE integrators might include Runge-Kutta methods, Adams methods, or others. For this work, we use an explicit Adams predictor-corrector method of second order to match the spatial algorithm. Detail concerning the implementation of these time integrators can be found for example in [28,24].

Focus now on the determination of one particular α, say $\alpha_{i+1/2,j}^n$. A linearization must be performed at the cell face and to accomplish this, an appropriate state must be chosen about which to perform that linearization. We choose the arithmetic average $\bar{\mathbf{u}} = \frac{1}{2}(\mathbf{u}_{i,j}^{\mathrm{td},n} + \mathbf{u}_{i+1,j}^{\mathrm{td},n})$. More sophisticated choices, such as the Roe state, could be made but in our experience this makes little difference in the eventual computed solutions. From this state, the linearization and eigenvalue decomposition $\mathbf{T}^{-1}\mathbf{\Lambda}\mathbf{T} = \mathbf{A} = \frac{\partial}{\partial \mathbf{u}}\mathbf{F}_1(\bar{\mathbf{u}})$ are found. Notice now that globally consistent notation has been abandoned in order to simplify the exposition. Whenever multiplication by $\mathbf{T}$ is performed to achieve characteristic quantities it should be understood that this implies linearization about a particular face, in this case $(i+1/2,j)$. For two dimensions, a large number of characteristic transformations must be performed (in three dimensions the number is even more drastic) and this constitutes the one of the most expensive parts of the FCT method.

In [4], DeVore indicates that the scheme of Zalesak does not preserve monotonicity in two dimensions and this fact was used as motivation for a more sophisticated pre-limiting strategy. There it is suggested to limit the fluxes using the original Boris/Book limiter [1,2] in each direction prior to their input to the multi-dimensional limiter. We have also found this to be a critical aspect of the algorithm and so it is implemented here. This is a rather simple device to implement and so we demonstrate it for just one flux, $\hat{\mathbf{F}}1_{i+1/2,j}^{\mathrm{AD},n}$, and leave the extension for the others to the reader. A straight forward extension of the Boris/Book limiter for this flux can be written as

$$\hat{\mathbf{F}}1_{i+1/2,j}^{\mathrm{AD},n} = s \max\left[0, \min\left(\left|\mathbf{T}\mathbf{F}1_{i+1/2,j}^{\mathrm{AD},n}\right|, s\frac{J_{i+1/2,j}\Delta r_1}{\Delta t}D_{+r_1}\mathbf{T}\mathbf{u}_{i+1/2,j}^{\mathrm{td},n}, s\frac{J_{i+1/2,j}\Delta r_1}{\Delta t}D_{+r_1}\mathbf{T}\mathbf{u}_{i-1/2,j}^{\mathrm{td},n}\right)\right] \tag{10}$$

where $s = \mathrm{sign}(\mathbf{T}\mathbf{F}1_{i+1/2,j}^{\mathrm{AD},n})$ and it is understood that (10) is to be interpreted component-wise. The "hat" notation indicates that the anti-diffusive flux has been pre-limited. The other $\hat{\mathbf{F}}$ fluxes are obtained through similar formulas.

To complete the description of the FCT algorithm in the overset grid context first define the local maximum and minimum characteristic values, $\mathbf{w}_{i,j}^{\mathrm{max}}$ and $\mathbf{w}_{i,j}^{\mathrm{min}}$ respectively, as

$$\mathbf{w}_{i,j}^{\mathrm{m},n} = \mathrm{m}\left(\mathbf{T}\mathbf{u}_{i-1,j}^{\mathrm{td},n}, \mathbf{T}\mathbf{u}_{i,j}^{\mathrm{td},n}, \mathbf{T}\mathbf{u}_{i+1,j}^{\mathrm{td},n}, \mathbf{T}\mathbf{u}_{i,j-1}^{\mathrm{td},n}, \mathbf{T}\mathbf{u}_{i,j+1}^{\mathrm{td},n}\right) \tag{11}$$

where "m" should be replaced by "max" and "min", the extrema are taken component-wise, and we should recall that maximum and minimum values must be found for the two states on either side of the cell face because $\mathbf{T}$ indicates linearization about that face. The results from (11) are the bounds for the characteristic quantities which

5

the eventual solution is not allowed to exceed. The actual influx into the cells on either side of the cell face which would result from the AD fluxes is computed for example as

$$\mathbf{I}_{i,j}^n = \frac{1}{\Delta r_1} D_{+r_1} \left[\max \left(\frac{\hat{\mathbf{F}}1_{i-1/2,j}^{\mathrm{AD},n}}{J_{i,j}}, 0 \right) \right] + \frac{1}{\Delta r_2} D_{+r_2} \left[\max \left(\frac{\hat{\mathbf{F}}2_{i,j-1/2}^{\mathrm{AD},n}}{J_{i,j}}, 0 \right) \right] \tag{12}$$

and the maximum permissible influx such that the characteristic bounds from (11) are not violated, indicated by the tilde, is for example

$$\tilde{\mathbf{I}}_{i,j}^n = \frac{1}{\Delta t} \left[\mathbf{w}_{i,j}^{\max} - \mathbf{T}\mathbf{u}_{i,j}^{\mathrm{td},n} \right]. \tag{13}$$

Component-wise ratios of permissible to actual fluxes are then defined for the two cells as

$$\mathbf{R}_{i,j}^{+,n} = \min \left(\frac{\tilde{\mathbf{I}}_{i,j}^n}{\mathbf{I}_{i,j}^n}, 1 \right). \tag{14}$$

The quantities $\mathbf{R}_{i,j}^{-,n}$, which represent the ratio of actual AD flux leaving the cell to the maximum flux permitted to leave the cell without violation of the bounds in (11), are defined using similar reasoning and computed as needed for both cells adjacent to the cell face. By choosing the most restrictive of these $\mathbf{R}$ values, the bounds from (11) are not violated. Thus we define

$$\beta = \begin{cases} \min(\mathbf{R}_{i,j}^{+,n}, \mathbf{R}_{i+1,j}^{-,n}) & \text{when} \quad J_{i,j}\hat{\mathbf{F}}1_{i+1/2,j}^{\mathrm{AD},n} < 0 \\ \min(\mathbf{R}_{i+1,j}^{+,n}, \mathbf{R}_{i,j}^{-,n}) & \text{when} \quad J_{i,j}\hat{\mathbf{F}}1_{i+1/2,j}^{\mathrm{AD},n} \geq 0. \end{cases} \tag{15}$$

The final values for $\alpha_{i+1/2,j}^n$ are found through component-wise inversion of the formula

$$\alpha_{i+1/2,j}^n \mathbf{F}1_{i+1/2,j}^{\mathrm{AD},n} = \mathbf{T}^{-1} \beta \hat{\mathbf{F}}1_{i+1/2,j}^{\mathrm{AD},n}. \tag{16}$$

It is important to note that monotonicity of the linearized characteristic variables does not imply monotonicity of the conserved variables. Thus the final updated solution could result in a negative density, imaginary sound speed, or negative pressure. Although rare, such occurrences can occur and must be treated in a rational and reasonable way. Zalesak suggests in [26,6] that a fail-safe limiter be employed and we take a similar approach here. At each time, if a given cell (i,j) violates physically realistic bounds after advancement to $\mathbf{u}_{i,j}^{\mathrm{new}}$ in (8), then no portion of the anti-diffusive flux is allowed at the boundaries of that cell. For such cells,

$$\alpha_{i+1/2,j}^n = \alpha_{i-1/2,j}^n = \alpha_{i,j+1/2}^n = \alpha_{i,j-1/2}^n = 0 \tag{17}$$

is enforced and the method becomes fully first order in a local region. In this paper, violations of physically realistic bounds are taken to be negative densities, negative pressures, or imaginary sound speeds. In our experience, this fail-safe mechanism is critical for the success of the FCT algorithm. It should also be noted that after setting $\alpha_{i\pm1/2,j\pm1/2}^n = 0$ in one cell, the problem (negative density etc.) may then appear in a neighbouring cell. In principle the result could be a cascade across all cells. To avoid this possibility we take a very simple approach and set all values of $\alpha_{i\pm1/2,j\pm1/2}^n$ over the entire domain to zero for such cases. A more sophisticated fail-safe procedure could be envisioned, but our experience shows that this is sufficient for a large class of problems. In terms of accuracy it should be noted that cases when the entire step reduces to first order are exceedingly rare and do not occur for any of the simulations presented in this work.

This completes the prescription of the FCT algorithm itself but there is another algorithmic aspect which must be addressed. In [26] it is recognized that some amount of higher order dissipation must be included in order to remove high frequency noise which has been generated by the FCT procedure. In that work the high order dissipation was added to the AD flux prior to flux correction. In our studies we found this to be unsatisfactory because some amount of the high order dissipation is removed by FCT unless the resulting values for the α's are
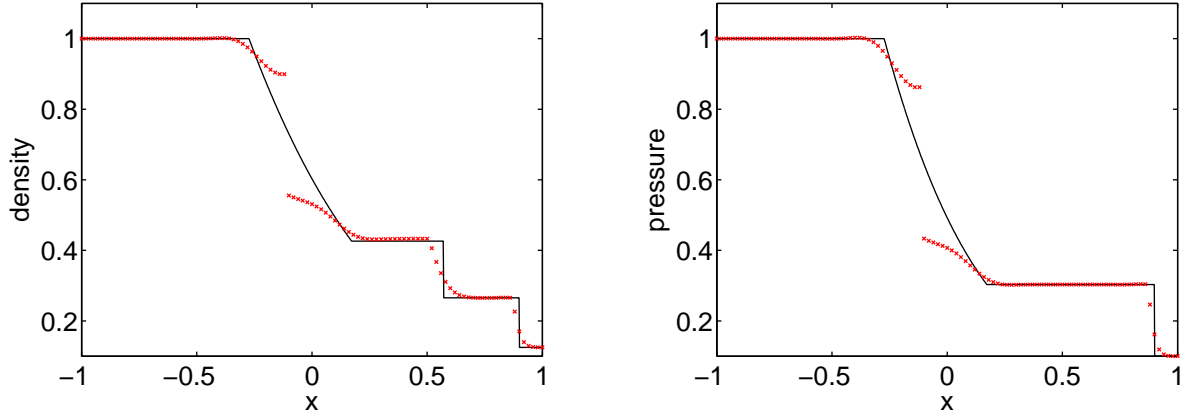
Fig. 1. FCT solution for a shock tube problem containing a sonic rarefaction. The black line represents the exact solution and the red crosses the numerical approximation at $t = 0.5$. The problematic behavior at the sonic point is quite clear in both the density (left) and pressure (right). (For interpretation of the references to color in this figure legend, the reader is referred to the web version of this article)

exactly one. The result is unacceptable levels of numerical noise in the computed solutions. Therefore we take the view that dissipation should be added independently after FCT. To this end we implement a second order dissipation near shocks [16,17,24] as well as a fourth order Jameson style dissipation away from shocks [29,30,24]. We switch the fourth order dissipation on or off based on density to ensure that it is not active near shocks or contacts. One final note is that the computed solution will not violate the prescribed bounds only for CFL numbers less than 1/2 and so all FCT simulation results presented in this paper set the CFL number to be 0.4.

3.3 Sonic fix

The next modification of the FCT algorithm that we introduce is the inclusion of a sonic fix that corrects the poor behaviour of the FCT algorithm at sonic points where local flow speed is equal to the speed of sound. As is the case for some other methods, such as Godunov's method with an approximate Roe Riemann solver, the FCT method can exhibit poor behavior near sonic points in rarefaction waves. To investigate this problem, Sod's shock tube problem [31,14] is modified in such a way to produce a sonic point inside the rarefaction wave of the solution. Table 1 shows the left and right states for this modified problem where a background translational velocity has been added so that the resulting rarefaction wave contains a sonic point. We compute approximations

	ρ	u_1	u_2	p
left	1.0	0.75	0.0	1.0
right	0.125	0.75	0.0	0.1

Table 1
Left and right states for a modified version of Sod's shock tube problem which includes a background translational velocity such that the rarefaction wave contains a sonic point.

to the solution of this Riemann problem using the grid $\mathcal{L}([-1, 1], 100)$ where

$$\mathcal{L}([x_a, x_b], N) = \{x_i \mid x_i = x_a + i\Delta x, \ \Delta x = (x_b - x_a)/N, i = 0, 1, \ldots, N\}, \tag{18}$$

with the initial discontinuity located at $x = -0.4$. Figure 1 shows the results produced by the FCT method. The problematic behavior of the method at the sonic point is clearly visible in the form of a rarefaction shock which represents an entropy violating weak solution and so is not acceptable.

There are some crucial differences between the problem illustrated in Figure 1 for the FCT method and the problem experienced with say Godunov's method and an approximate Roe Riemann solver. The existence of rarefaction shocks in numerical approximations is typically the result of insufficient numerical diffusion. For FCT this is caused by the use of centered fluxes but the underlying first order monotone method does not exhibit problematic behavior at sonic points. This is in contrast to Roe's method where the problem at sonic points in rarefactions is exhibited even for the first order method because the source is the Roe linearization itself. We will rely on the fact that the first order method used in the FCT solver does not produce rarefaction shocks and simply set the value for α in (8) to zero for cases where sonic rarefactions are present. Of course this choice has implications on solution accuracy, but because sonic points exist in isolation, the impact is negligible as will be demonstrated in Section 4. There may be other more elegant methods to combat the difficulty of sonic points in rarefaction waves, but for the simulations in this work we have found our choice to be satisfactory.

To describe our sonic fix, begin by noting that any anti-diffusive flux in (8) has left and right state associated with it, call these $\mathbf{u}_L$ and $\mathbf{u}_R$ respectively. For instance consider $\mathbf{F}_{1_{i+1/2,j}}^{\mathrm{AD},n}$ and set $\mathbf{u}_L = \mathbf{u}_{i,j}^{\mathrm{td},n}$ and $\mathbf{u}_R = \mathbf{u}_{i+1,j}^{\mathrm{td},n}$. These states can be viewed as left and right states of a one dimensional Riemann problem in the direction normal to the cell face. If the cell face unit normal is defined as $\mathbf{n} = (n_1, n_2)$, define the normal velocities as $v_{n,L} = \mathbf{n} \cdot \mathbf{u}_L$ and $v_{n,R} = \mathbf{n} \cdot \mathbf{u}_R$. Following the nomenclature in [14], we define the star state as the center solution to this Riemann problem (i.e. the solution between the c^+ and c^- characteristics). As in [14], p^* and v_n^* can be approximated by

$$p^* = \sqrt{\max\left(0, \frac{c_L + c_R - \frac{\gamma-1}{2}(v_{n,R} - v_{n,L})}{\frac{c_L}{p_L^z} + \frac{c_R}{p_R^z}}\right)} \tag{19}$$

and

$$v_n^* = v_{n,L} + \frac{2}{\gamma - 1}(c_L - c_L^*) \tag{20}$$

where $c_L^* = c_L(p^*/p_L)^z$, $c_R^* = c_R(p^*/p_R)^z$, $z = \frac{\gamma-1}{2\gamma}$, c_L is the left sound speed, and c_R is the right sound speed. These particular star states arise from the approximation of the Riemann solution by the so-called two rarefaction Riemann solver and can be viewed as an approximation to the true star state. In this work, we use the approximate star states defined by (19) and (20) to indicate a sonic point, but this is by no means the only acceptable approximation for these quantities. Given the star states, the sonic fix we employ is to set a provisional value for α, call it $\tilde{\alpha}$, as

$$\tilde{\alpha}_{i+1/2,j}^n = \begin{cases} 0 & \text{if} & v_{n,L} - c_L \leq 0 \quad \text{and} \quad v_n^* - c_L^* \geq 0 \\ 0 & \text{if} & v_n^* + c_R^* \leq 0 \quad \text{and} \quad v_{n,R} + c_R \geq 0 \\ \alpha_{i+1/2,j}^n & \text{else.} \end{cases}$$

Now α is set to that provisional value as

$$\alpha_{i+1/2,j}^n = \tilde{\alpha}_{i+1/2,j}^n.$$

The effect of these choices is to return the solver to first order accuracy near sonic points in rarefaction waves. Figure 2 shows the solution to the modified Sod's problem of Table 1 employing this sonic fix. Here it is seen that the poor behavior demonstrated in Figure 1 has been effectively eliminated. The solution does still contain a small kink at the sonic point, but the bulk behavior has been fixed.

3.4 Strong Rarefactions

In addition to the poor behavior for sonic rarefaction waves, the traditional FCT algorithm seems to run into difficulties for rarefaction waves where the difference in velocities at which the gas is being pulled apart differ by more than the local sound speed. This is actually a very difficult problem for many methods because a near vacuum state is reached and many methods fail at these points [5]. Rarefactions such as these are sometimes
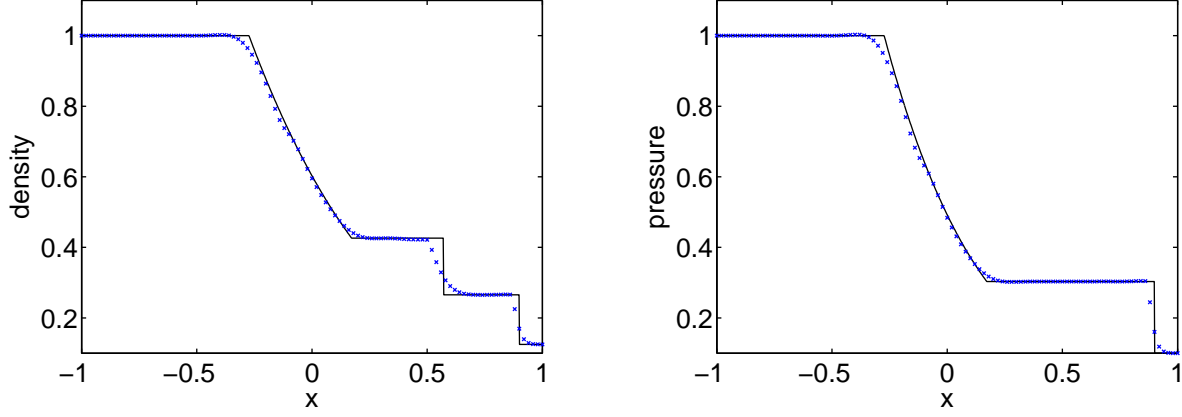
Fig. 2. FCT solution including the sonic fix for a shock tube problem containing a sonic rarefaction. The black line represents the exact solution and the blue crosses the numerical approximation at $t = 0.5$. The problematic behavior seen in Figure 1 has been effectively eliminated. Both the density (left) and pressure (right) are well behaved and agree nicely with the exact solution near the sonic point. (For interpretation of the references to color in this figure legend, the reader is referred to the web version of this article)

	ρ	u_1	u_2	p
left	1.0	-2.0	0.0	0.4
right	1.0	2.0	0.0	0.4

Table 2
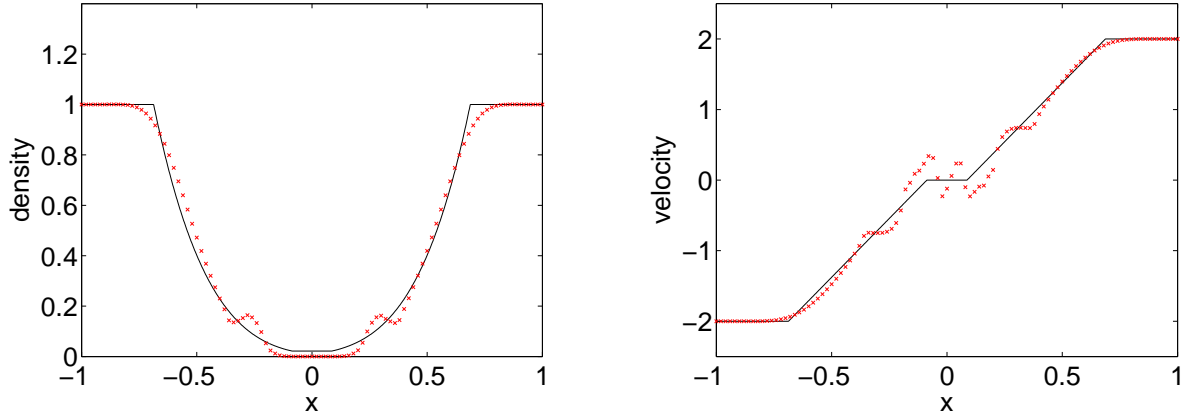Left and right states for a strong rarefaction Riemann problem.

Fig. 3. Density (left) and velocity (right) or the strong rarefaction problem of Table 2 at $t = 0.25$. The black line represents the exact solution and the red crosses the numerical approximation. The oscillations in velocity are particularly troubling but also note the undershoot of the density near the origin. (For interpretation of the references to color in this figure legend, the reader is referred to the web version of this article)

referred to as strong rarefaction waves and a simple Riemann problem which exhibits this behavior is given in Table 2. For this problem, the near vacuum center state causes difficulty for the FCT algorithm as well as many other Eulerian type methods. Figure 3 shows the density and velocity as computed by the FCT algorithm for this case and clearly shows the oscillations in velocity in the near vacuum state (near the origin). In order to remove this behavior a simple fix is employed which sets
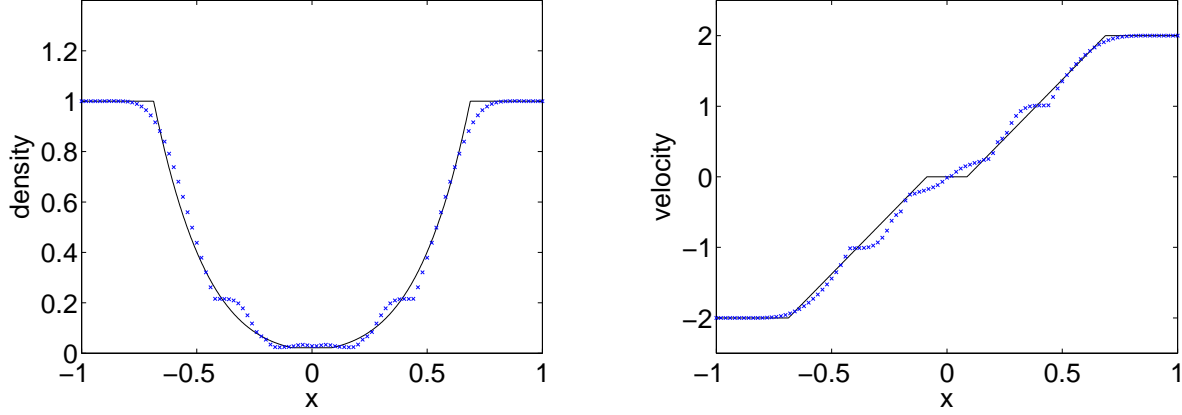
$$\alpha^n_{i+1/2,j} = 0$$

Fig. 4. Density (left) and velocity (right) for the strong rarefaction problem of Table 2 at $t = 0.25$ including the fix for strong rarefactions. The black line represents the exact solution and the blue crosses the numerical approximation. The oscillations in velocity have been removed and the density adhears much more closely to the exact solution. (For interpretation of the references to color in this figure legend, the reader is referred to the web version of this article)

if

$$p^* < \min(p_L, p_R) \quad \text{and} \quad |v_{n_L} - v_{n_R}| \geq \max(c_l, c_r).$$

This causes the first order scheme to be used when strong rarefaction waves are present. Figure 4 shows the results of the FCT algorithm including this fix. The velocity is monotonic and well behaved near the origin. These results are comparable to the results of Tóth in [5]. Clearly the FCT method, even after inclusion of this fix, is not perfect and there is certainly room for improvement, but the inclusion of this fix is a step in the right direction and is used throughout this work.

3.5 A note concerning monotonicity

An interesting issue which is not discussed in the literature is the fact that the FCT method of Zalesak is not provably a monotone method. The implementation in this paper mirrors the implementation of Zalesak and so it also lacks a proof of monotonicity. In fact we present a simple problem for which the Zalesak implementation of FCT produces non-monotone results. To demonstrate this violation consider the following example. Take the particular case of linear advection with unit advection velocity. This is a special case of (1) found by setting uniform pressure, unit velocity in the x_1-direction and no velocity in the x_2-direction. For this case the governing equations reduce to

$$\frac{\partial}{\partial t}\rho + u\frac{\partial}{\partial x_1}\rho = 0.$$

We are working temporarily in 1-D and so we use simplified notation. Application of FCT to this simple system requires the low order flux which is given simply as the upwind flux $\mathbf{f}^{\text{low},n}_{i+1/2} = u\rho^n_i$, and the second order centered flux $\mathbf{f}^{\text{high},n}_{i+1/2} = u\frac{1}{2}(\rho^n_i + \rho^n_{i+1})$. At time level t^n let the approximate solution be given by

$$\rho^n_{-3} = 4.5, \quad \rho^n_{-2} = 4, \quad \rho^n_{-1} = 3.5, \quad \rho^n_0 = 3, \quad \rho^n_1 = 3, \quad \rho^n_2 = 2, \quad \rho^n_3 = 1, \quad \rho^n_4 = 0.$$

Set the grid spacing as $\Delta x_1 = 1$, the temporal spacing as $\Delta t = 0.25$ and impose unit translational velocity $u = 1$. The FCT algorithm, as outlined by Zalesak [26,27], produces the following values for α

$$\alpha^n_{-1/2} = 1, \quad \alpha^n_{1/2} = 1, \quad \alpha^n_{3/2} = 1.$$

By using the forward Euler time integrator (i.e. $\rho^{n+1}_i = \rho^{\text{new}}_i$), the FCT solution after a single step results in the values

$$\rho^{n+1}_0 = 3.0625, \quad \rho^{n+1}_1 = 3.125.$$

The solution at time t^n was monotonically decreasing left to right while the solution for these two cells at time t^{n+1} is monotonically increasing left to right and so the failure of the algorithm is clear. Many authors suggest the use of a pre-limiter, but for this case the pre-limiter suggested by Zalesak [26] and Kuzmin [6] has no effect as can be easily verified. The pre-limiter of DeVore [4], which we have adopted here, does remedy this particular problem, but a proof of monotonicity for arbitrary high order fluxes remains elusive.

4   Numerical Results

We now present simulation results using the FCT algorithm described in Section 3. The discussion centers on studying the robustness and accuracy of the overall numerical approach. To this end we compare results to those from a high-resolution Godunov method. This comparison is made in order to provide a relative idea of the expected performance of the FCT method as it compares to more rigorously tested methods. In concert with the results provided for example in [22], one can place high-resolution Godunov methods, WENO methods, and FCT in relation to each other. The exact implementation of the Godunov method used here is the subject of the previous work in [16–18].

We note that the expected convergence rate for FCT has been established using the method of analytic solutions. This test was also performed for the Godunov method as in [18]. However, the value of comparing the results between the two methods for such a contrived example is limited and instead we jump straight to a number of classic 1-D high-speed flow examples. These include isolated contacts, Sod's shock tube problem, a two-shock Riemann problem, and the Shu-Osher test case. The methods are then compared on a number of 2-D problems including shock impingement on a cylinder, and the irregular Mach reflection of a strong shock on an inclined ramp.

4.1   Isolated Contact and Shock Discontinuities

4.1.1   Contact wave

The contact wave, which is an admissible solution to (1), is a discontinuous linear jump and as such is a relatively difficult case for non-compressive shock capturing schemes. The difficulty is manifest as sub-linear convergence rates for the L_1 norm (shock capturing methods such as the ones under consideration do not converge in an L_∞ sense for discontinuous solutions because order 1 errors are always present for at least one point). For linear waves, the characteristics run parallel and error is allowed to accumulate near jumps. The result is that a nominally N^{th} order non-compressive shock capturing scheme converges with a rate of $N/(N+1)$ in the L_1 sense [32–34]. The construction of the FCT method does not immediately indicate if the scheme should be compressive or not and this test is meant to establish that characterization.

For the contact wave, define a one-dimensional discontinuous initial condition with left and right states shown in Table 3. The exact solution to this problem (for $\gamma > 1$) consists of a propagating discontinuity, moving to the

	ρ	u_1	u_2	p
left	0.1	1.0	0.0	1.0
right	1.0	1.0	0.0	1.0

Table 3
Left and right states for a Riemann problem whose solution is a contact discontinuity traveling to the right with speed 1.0.

right with speed 1.0. The density jumps through this discontinuity but the pressure and velocity remain constant. Simulations are performed on the grid defined by $\mathcal{L}([0.0, 1.0], 200m)$ where m is a measure of grid resolution. Initial conditions for this Riemann problem consist of a jump located at $x_0 = 0.25$ and the appropriate left and right states from Table 3 are applied on either side. Boundary conditions are required at the endpoints of the interval,

11

and for this test case the exact solutions is applied when needed. Although the solution is valid for $\gamma > 1$, we choose the specific value $\gamma = 1.4$ which corresponds to a diatomic gas such as air.

A convergence study is performed at various numerical resolutions indicated by m with the comparisons taking place at $t_f = 0.5$ using the discrete L_1 norm. Results from this study are given in Table 4 where the convergence rate κ is estimated through a least squares fit as before. Here it is seen that both the FCT and

m	$e_\rho(m)$ F	$e_\rho(m)$ G
1	1.06e$-$2	1.39e$-$2
2	6.64e$-$3	8.78e$-$3
4	4.18e$-$3	5.55e$-$3
8	2.63e$-$3	3.51e$-$3
κ	.67	.66

Table 4
Convergence results for the contact wave problem using second order Godunov and FCT approximations, indicated by "F" and "G" in the headings respectively. L_1 errors in density at $t_f = 0.5$ for grid resolutions determined by m, and the estimated convergence rate κ found through a least squares fit. Note that errors for velocity and pressure are identically zeros and so are not shown.

Godunov methods demonstrate convergence at the rate of $\kappa \approx 2/3$ which determines that both schemes are in fact non-compressive second order high-resolution schemes. We can also see that the FCT method captures the contact with approximately 30% less error than the Godunov method for a given resolution. Smaller error for FCT is not entirely surprising as it is constructed to produce as little smearing as possible while attempting to maintain monotonicity. Note that the Godunov results are sensitive to which Riemann solver is used (here it is Roe's solver [14]) and which limiter is used (here it is minmod [14]). These choices represent a relatively standard implementation of the high-resolution Godunov method. The use of other limiters is particularly important and the reader is referred to [34] for further discussion on this point. Still it is worth noting that the FCT method does have more resolving power for this linear wave test problem than does Godunov's method using Roe's solver and the minmod limiter. Furthermore it is valuable to know that the FCT procedure outlined in this paper results in a non-compressive scheme.

4.1.2   Shock wave

The second admissible solution to (1) consisting of a pure jump is that of a shock wave. Such solutions can be constructed with reference to [35] for example, and are typically parameterized by the Mach number M of the shock in relation to the quiescent flow ahead of the propagating shock. Picking a particular value for M, as well as a complete pre-shock state, defines the flow for a particular γ. For this study set $M = 2$ and $\gamma = 1.4$ corresponding to air. The pre- and post-shock states are given in Table 5. Because this is a nonlinear phenomenon,

	ρ	u_1	u_2	p
left	2.67	1.48	0.0	4.50
right	1.0	0.0	0.0	1.0

Table 5
Left and right, pre- and post-shock respectively, states for a Riemann problem whose solution is a $M = 2$ shock discontinuity in air with $\gamma = 1.4$, traveling to the right with speed ≈ 2.366.

the characteristic curves do not run parallel to the discontinuity but rather enter into it. This acts as a steepening mechanism and so error is not allowed to accumulate and diffuse the jump as was the case for the contact wave in

Section 4.1.1 above. However, because capturing schemes always result in order 1 errors near jumps convergence is again gauged using the discrete L_1 norm. Computations are carried out on the unit interval $x \in [0,1]$ using mesh $\mathcal{L}([0.0, 1.0], 200m)$ with m being a measure of grid resolution. The exact solution is applied where boundary conditions are required. The initial jump is placed at $x_0 = 0.25$ and integration is carried out to time $t_f = 0.25$ where comparison to the exact solution is performed. The results are presented in Table 6.

m	$e_\rho(m)$ F	$e_\rho(m)$ G	$e_{u_1}(m)$ F	$e_{u_1}(m)$ G	$e_p(m)$ F	$e_p(m)$ G
1	8.38e−3	7.08e−2	5.59e−3	4.83e−3	1.44e−2	1.26e−2
2	3.94e−3	3.65e−3	2.91e−3	2.76e−3	6.57e−3	6.35e−3
4	2.08e−3	1.82e−3	1.39e−3	1.22e−3	3.63e−3	3.27e−3
8	9.63e−4	9.15e−4	7.13e−4	6.72e−4	1.66e−3	1.60e−3
κ	1.03	0.99	1.00	0.97	1.02	0.99

Table 6

Convergence results for the shock wave problem using second order Godunov (G) and FCT (F) approximations. L_1 errors in density, velocity and pressure at $t_f = 0.25$ for grid resolutions determined by m, and the estimated convergence rate κ found through a least squares fit.

Both schemes demonstrate first order convergence, $\kappa \approx 1$, in the least squares fit of the convergence rate for density, velocity and pressure which implies that both schemes capture the shock discontinuity with a constant number of grid points at all resolutions. Contrast this to the case of the contact above where the captured discontinuity contained an increasing number of grid cells even as its overall width decreased. For this $M = 2$ shock test case, both the second order Godunov and FCT schemes demonstrate convergence rates of $\kappa \approx 1$. Furthermore, the Godunov method demonstrates $\approx 10\%$ less error for this $M = 2$ case.

4.2 Sod's shock tube problem (modified)

Another classic test problem for high-speed flow solvers is the so called "Sod" shock tube problem [31,14]. This problem is meant to model the one-dimensional flow resulting from the rupture of a membrane separating air of differing density and pressure inside a shock tube. Mathematically this amounts to the solution of a Riemann problem for a $\gamma = 1.4$ ideal gas with particular left and right states. Part of the the advantage of using this test problem is that an exact solution exists and can be readily found (see [35,14] for details) and this enables a detailed comparison between the approximate results and the exact solution. We use a slightly modified version of the classic Sod problem in that a uniform translational velocity is added so that the resultant rarefaction wave is trans-sonic and the sonic fixes for both algorithms are used and tested. This problem was also used in section 3.3 during the development of the sonic fix for the FCT scheme and table 1 shows the left and right states. Details concerning the sonic fix for the Godunov scheme can be found in [14]. The computational domain is again chosen to be $x \in [-1, 1]$, the initial jump is placed at $x_0 = -0.4$, and the governing equations (1) are integrated in time to $t_f = 0.5$. As before the computational grid for this study is given by $\mathcal{L}([-1.0, 1.0], 100m)$ where m again measures grid resolution. The exact solution is applied at boundaries as required.

The exact density and pressure, as well as approximate results for $m = 1$ for both the Godunov and FCT methods, are shown in Figure 5 which demonstrates the similarity of the two approximate solutions. The primary difference between the two approximate solutions is the slight overshoot in velocity exhibited by the FCT method behind the lead shock. This trend continues for all resolutions but is more easily seen for this coarse simulation where $m = 1$. Figure 5 also shows that both methods seems to be handling the sonic rarefaction with their associated fixes as well as approximating the global solution character reasonably well. Quantitative convergence results are shown in Table 7 using the discrete L_1 norm. These results indicate that although both schemes are clearly converging to the exact solution, neither scheme is yet in the asymptotic range of convergence where the
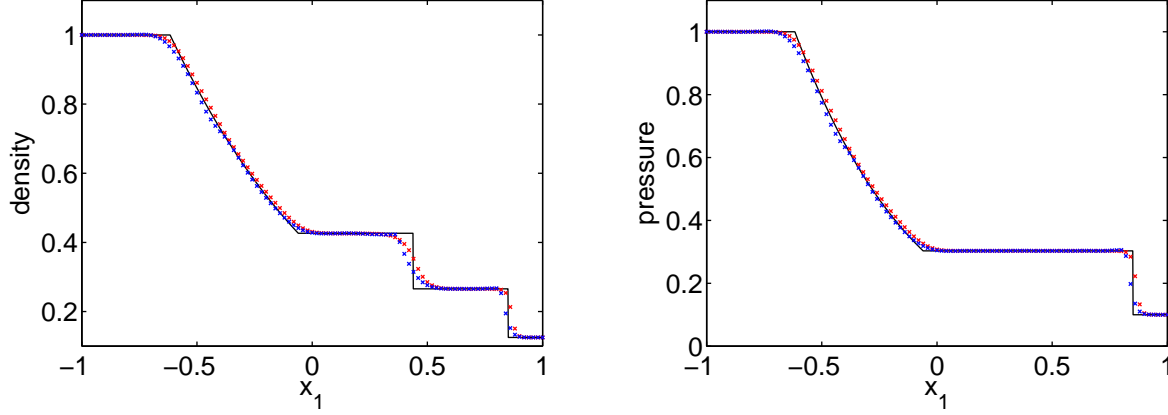
13

Fig. 5. Exact solution (black line) and numerical approximations with $m = 1$ for Godunov's method using Roe approximate Riemann solver (red marks) and the FCT method (blue marks) for the modified Sod shock tube problem at $t_f = 0.5$. Shown here are the density (left) and the pressure (right). (For interpretation of the references to color in this figure legend, the reader is referred to the web version of this article)

m	$e_\rho(m)$ F	$e_\rho(m)$ G	$e_{u_1}(m)$ F	$e_{u_1}(m)$ G	$e_p(m)$ F	$e_p(m)$ G
2	8.86e−3	9.44e−3	1.44e−2	1.44e−2	6.54e−3	6.32e−3
4	5.00e−3	5.31e−3	6.99e−3	7.51e−3	3.21e−3	3.22e−3
8	3.05e−3	3.03e−3	3.32e−3	4.08e−3	1.54e−3	1.67e−3
16	1.83e−3	1.80e−3	1.59e−3	2.42e−3	7.24e−4	9.08e−4
κ	0.76	0.80	1.06	0.86	1.06	0.93

Table 7
Convergence results for the modified Sod shock tube problem. Discrete L_1 error and associated least squares fit convergence rate κ for the Godunov (G) and FCT (F) schemes at selected resolutions associated with the choice of m. Apparently the mesh is of insufficient resolution for the methods to exhibit global convergence rates of $2/3$ for the L_1 norm of density which is dictated by the captured contact. However, both schemes exhibit convergence to the exact solution with the FCT method providing somewhat higher rates for pressure and velocity.

L_1 error of density will be dominated by the $2/3$ convergence rate near the contact. Even so, both schemes provide similar convergence behavior with the FCT yielding slightly higher convergence rates for the pressure and velocity and thus smaller error measures particularly for the higher resolutions.

4.3 A Two-Shock Riemann Problem

The last Riemann problem investigated in this work is commonly know as the two-shock problem. The solution to this problem for $\gamma = 1.4$ has a $M \approx 5.62$ shock in the rightmost characteristic field, a $M \approx 1.81$ shock in the leftmost characteristic field, and a contact wave separating the two. Left and right states for this problem are taken from [14] and shown in Table 8. The exact solution is again determined as in [35], and for the choice of translational velocity reflected in Table 8 results in a nearly stationary shock for the leftmost characteristic field. The actual speed of the left shock is $S \approx 0.78$, the velocity through the contact wave is $u_1 \approx 8.69$, and the rightmost shock moves with speed $S \approx 12.25$. The nearly stationary shock proves to be one of the primary difficulties for numerical approximations in this problem. The other difficulty for shock capturing schemes is the severity of the jump through the contact, and the need to accurately resolve that jump before reasonable global approximation is achieved.

14

	ρ	u_1	u_2	p
left	5.99242	19.5975	0.0	460.894
right	5.99242	-6.19633	0.0	46.0950

Table 8
Left and right states for the two-shock Riemann problem with $\gamma = 1.4$. The exact solution to this problem consists of a $M \approx 5.62$ shock in the rightmost characteristic, a $M \approx 1.81$ shock in the leftmost characteristic, and a contact wave separating the two.
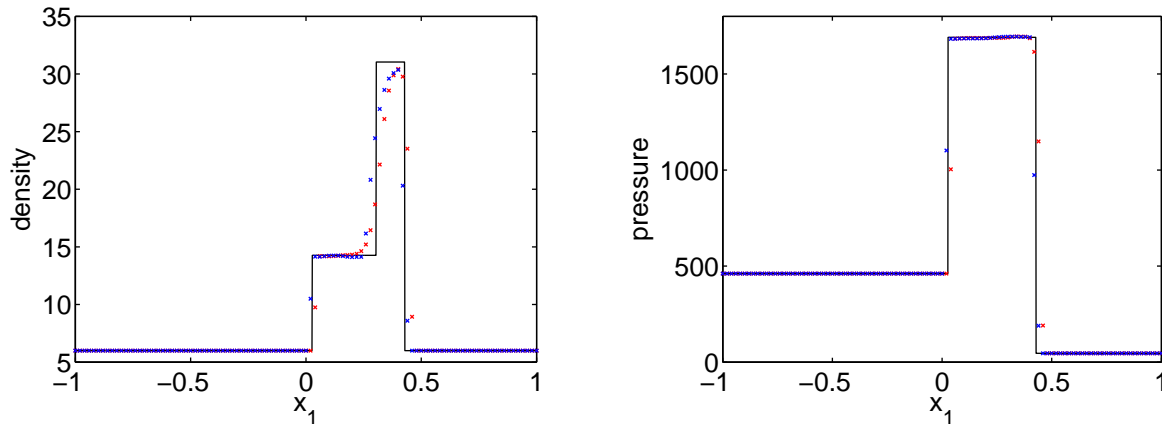

Fig. 6. Exact solution (black line) and approximations with $m = 1$ for Godunov's method using Roe approximate Riemann solver (red marks) and the FCT method (blue marks) for the two-shock Riemann problem at $t_f = 0.035$. Shown here are the density (left) and the pressure (left). (For interpretation of the references to color in this figure legend, the reader is referred to the web version of this article)

The solution for this problem is approximated for $x \in [-1, 1]$ using the mesh $\mathcal{L}([-1.0, 1.0], 100m)$ with m a measure of grid resolution. The exact solution is applied at boundaries where required and integration is carried out to a final time of $t_f = 0.035$. Figure 5 shows the exact density and pressure at that time as well as the numerical approximations for $m = 1$. Qualitatively it is seen that the two schemes behave nearly identically. However, close inspection revels the Godunov approximation to be slightly less oscillatory particularly in the pressure while the FCT approximation shows a sharper capture of the contact wave. Table 9 shows quantitative convergence results for the two schemes using the discrete L_1 norm for the computation of the errors. This table shows that the

m	$e_\rho(m)$ F	$e_\rho(m)$ G	$e_{u_1}(m)$ F	$e_{u_1}(m)$ G	$e_p(m)$ F	$e_p(m)$ G
2	4.48e-1	7.53e-1	1.10e-1	3.40e-1	8.74e0	3.29e1
4	2.58e-1	4.08e-1	7.15e-2	1.41e-1	6.49e0	1.40e1
8	1.51e-1	2.26e-1	2.48e-2	7.78e-2	3.34e0	7.89e0
16	9.00e-2	1.43e-1	1.66e-2	4.76e-2	1.82e0	4.94e0
κ	0.77	0.80	0.91	0.94	0.75	0.90

Table 9
Discrete L_1 error and associated least squares fit convergence rate κ for the two shock problem using the Godunov (G) and FCT (F) schemes at selected resolutions associated with the choice of m. Neither scheme is yet in the asymptotic range of convergence where the L_1 errors in density will be dominated by the $2/3$ convergence rate at the contact. Both schemes exhibit convergence to the exact solution with neither scheme substantially outperforming the other in terms of error.

15

Godunov approximations demonstrate somewhat higher convergence rates for all quantities, but that for these resolutions the FCT approximations always result in smaller actual errors. In fact for the pressure and velocity, the errors in the FCT approximations are more than three times smaller than the Godunov approximations at coarse resolutions and still more than twice as small for the finest mesh considered.

4.4 Shu-Osher Problem

The final one-dimensional test case considered in this paper is a problem originally considered by Shu and Osher [7] and subsequently by others [22,23]. This problem consists of a $M = 3$ shock in air, $\gamma = 1.4$, traveling into unshocked air with sinusoidally perturbed density. As originally presented, the problem has a number of parameters and the specific values used here are taken from [22]. Equation (21) shows the initial setup where the parameter values are $\epsilon = 0.2$ and $\lambda = 5$.

$$\begin{aligned} \rho = 3.857143, \quad & u_1 = 2.629369, \, u_2 = 0, \, p = 10.33333 \quad && \text{for } x_1 < -4 \\ \rho = 1 - \epsilon \sin\left(\lambda \pi x\right), \, u_1 = 0, \quad & u_2 = 0, \, p = 1 \quad && \text{for } x_1 \geq -4 \end{aligned} \tag{21}$$

The approximate solution is computed for $x \in [-5, 5]$ and integrated to a final time $t_f = 1.8$. Computationally this is achieved using $\mathcal{L}([-5.0, 5.0], 200m)$ where m again measures grid resolution. There is no known closed form exact solution to this problem and so the exact solution used for comparison must be found through other means. Here we choose a very finely resolved simulation and refer to this as the reference solution. The authors in [22] used a third method to compute the reference solution but we take a slightly different approach. For this paper, each method is used to compute a very high resolution approximate solution which will be used as the reference solution for convergence studies of that method. Thus the FCT method is used to compute the reference solution for convergence study of FCT, and the Godunov method is used to compute the reference solution for convergence study of Godunov's method.

When interpreting results, it is useful to understand the Riemann structure of the solution when $\epsilon = 0$. For this case we can determine an exact solution and the waves present there give a good indication where structures in the more complicated solution will arise. When $\epsilon = 0$, the solution consists of a $M = 3$ shock traveling with speed $S \approx 3.55$, but the solution also contains a contact traveling with speed $S \approx 2.63$ and a left acoustic wave with traveling with speed $S \approx 0.69$. These latter two waves have no strength and so no variation occurs through them, but the solution to the perturbed problem with $\epsilon \approx 0$ will see disturbances traveling close to these characteristic speeds. At $t = 1.8$, the lead shock in this analysis will have travelled to $x_1 \approx 2.39$, the contact wave to $x_1 \approx 0.73$ and the left acoustic wave to $x_1 \approx -2.76$. For small ϵ it is expected that the exact solution will change character near these locations.

The reference solution is computed with $m = 128$ at $t = 1.8$ and can be seen for example in figure 7. It is seen that for $x < -2.76$ the solution is the unperturbed post-shock state. For $x \in (-2.76, 0.73)$ the solution exhibits mild oscillations in all quantities. These oscillations are the result of the passage of the left acoustic wave. For $x \in (0.73, 2.39)$ the solution exhibits what looks to be chaotic behavior in the density but is actually highly resolved oscillations. The statement that these are well resolved is evidenced by the fact that further refinement does not change the character of the solution in any way, although we do not present more refined results. That is to say that this resolution, $m = 128$, is sufficient to be in the regime of asymptotic convergence. For $x > 2.39$ the solution returns to the initial upstream state. The locations where the solution changes behavior are, as expected, those mentioned above in the discussion of the Riemann structure for $\epsilon = 0$. Notice further that the transition to high frequency oscillations in density occurs exactly at the location of the contact wave.

The difficulty in computing approximations to this problem comes from the fact that high resolution is required to accurately represent the high frequency oscillations that occur for $x \in (0.73, 2.39)$. In [22], the authors takes the view that because cell averaged quantities are being evolved by the numerical methods, convergence of the schemes should be measured with respect to errors in those cell averaged quantities. This is indeed a fair comparison, but we take a slightly different standpoint and use pointwise convergence. Our reasoning is that a perfect cell averaged quantity, one with zero error, would say nothing of the solution structure within that cell.

For problems where the solution is highly oscillatory and one is interested in an accurate representation of those oscillations, pointwise convergence is a more instructive quantity to investigate. Also note that the cell average is a second order approximation to the point value at the cell center and so no conversion is required to convert from average to point quantities when 2nd order schemes, such as the ones under consideration, are used. When sufficient resolution for asymptotic convergence is reached, it is unlikely that two methods, convergence pointwise or by cell averages, will differ in any substantial way and the convergence rates will necessarily tend to the same value.

Table 10 shows the pointwise convergence results in the discrete L_1 norm for both the FCT and Godunov schemes. From this table it is clear that the coarser resolutions do not approximate the solution well at all,

m	$e_\rho(m)$ F	r	$e_\rho(m)$ G	r	$e_{u_1}(m)$ F	r	$e_{u_1}(m)$ G	r	$e_p(m)$ F	r	$e_p(m)$ G	r
1	1.11e0	–	1.03e0	–	3.43e−1	–	2.97e−1	–	2.32e0	–	1.94e0	–
2	8.75e−1	0.34	8.62e−1	0.25	1.54e−1	1.2	1.50e−1	0.99	1.06e0	1.1	1.04e0	0.90
4	7.49e−1	0.22	7.51e−1	0.20	6.09e−2	1.3	7.36e−2	1.0	4.57e−1	1.2	5.33e−1	0.96
8	5.69e−1	0.40	6.42e−1	0.22	2.87e−2	1.1	3.77e−2	0.96	2.07e−1	1.1	2.63e−1	1.0
16	2.14e−1	1.4	4.36e−1	0.56	1.38e−2	1.1	2.04e−2	0.88	9.75e−2	1.1	1.50e−1	0.81
32	7.00e−2	1.6	1.71e−1	1.4	5.74e−3	1.3	1.01e−2	1.0	3.65e−2	1.4	6.85e−1	1.1

Table 10
Convergence results for the Shu-Osher test problem using both the Godunov (G) and FCT (F) methods. Because the solutions at low resolution cannot approximate the true solution, a least squares fit to the convergence curve is not appropriate. Instead we use the computed convergence rates at each resolution $(\log(e(m-1)/e(m))/\log(2))$, where $e(m)$ is computed relative to the reference solution.

particularly for the density, and very low rates of convergence are attained. Figure 7 demonstrates this graphically where the numerical approximations for $m = 1$ are plotted on top of the reference solution. In this figure it is clear that neither solution does a particularly good job at resolving the high or low frequency oscillations. For low resolutions, it would appear that the Godunov method provides a more accurate approximation as is reflected in Table 10. For higher resolutions, the FCT method provides a more accurate representation of the solution, particularly the high frequency oscillations. For instance take the case with $m = 16$ shown in Figure 8. At this resolution the FCT method is beginning to approximate the oscillations for $x \in (0.73, 2.39)$ while Godunov's method is still having substantial difficulty. This is also reflected in Table 10. In general for low resolutions, the high frequency oscillations are simply not captured and both methods exhibit poor convergence properties, particularly for the density. For both methods this means convegence at some low rate ≈ 0.3. For some critical resolution however, both methods see a rise in convergence rates, tending to some value larger than 1. For FCT this transition to higher convergence rates happens at lower resolution, indicating that the FCT method has more resolving power than the Godunov method. For the highest resolutions demonstrated here, both approximations have entered their asymptotic range and their convergence rates becomes roughly equal. However, because the FCT method experienced the transition to higher convergence rates earlier in the refinement process, the errors at the highest resolutions are smaller than for the Godunov approximations by nearly a factor of 2.

4.5 Shock Impingement on Stationary Cylinder

For two dimensions, one finds that problems with known exact solutions are difficult to develop. The method of manufactured solutions can be used to verify the implementation of a numerical method, but the practical value of comparing two methods head to head for such a contrived example is limited. These solutions typically have very little resemblance to the flows that the methods have been designed to simulate and so it is unclear what information would be gained through such a comparison. Instead we present results for some classic two
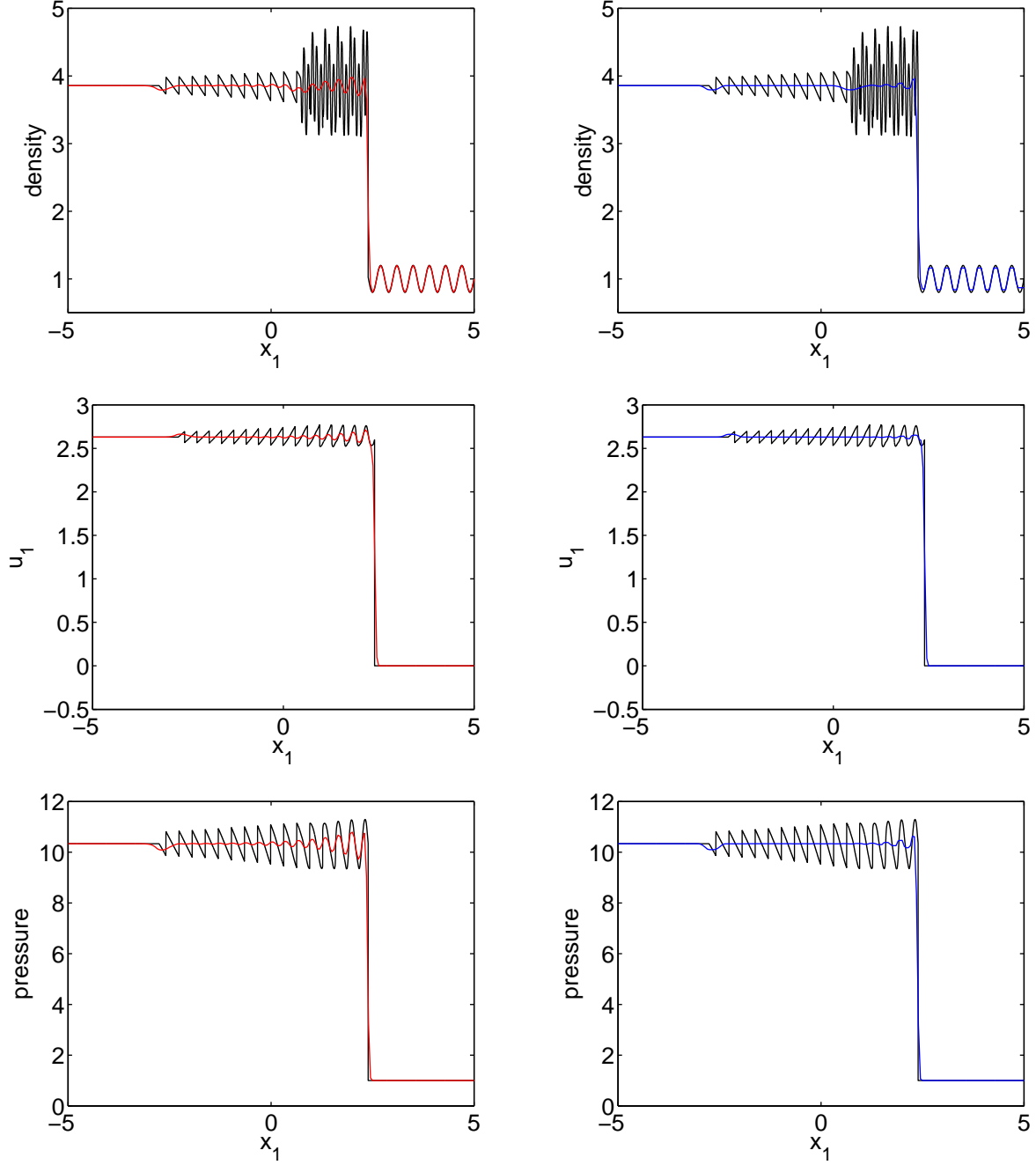
Fig. 7. Comparison of the numerical approximations with $m = 1$ at $t = 1.8$ for the Shu-Osher test problem. For both images the black line represents the reference solution while the red line (left) shows the Godunov approximation and the blue line (right) shows the FCT approximation. From top to bottom are density, velocity, and pressure. (For interpretation of the references to color in this figure legend, the reader is referred to the web version of this article)

dimensional high-speed flow problems with no known exact solution, but for which sufficient data exists in the literature to render them reasonable test problems.

The first test problem which we consider is the impingement of a $M = 2$ shock on a rigid immovable cylinder. The basic problem consists of a rigid cylinder of radius 0.5 placed in the larger domain $[-2, 2] \times [-2, 2]$. Initially, there is a Mach 2 shock located at $x_1 = -1.5$ running from left to right. The computational mesh is defined as the overlapping mesh constructed from $\mathcal{A}((0, 0), [0.5, 1.0], 10m, 80m)$ and $\mathcal{R}([-2, 2] \times [-2, 2], 80m, 80m)$ where m
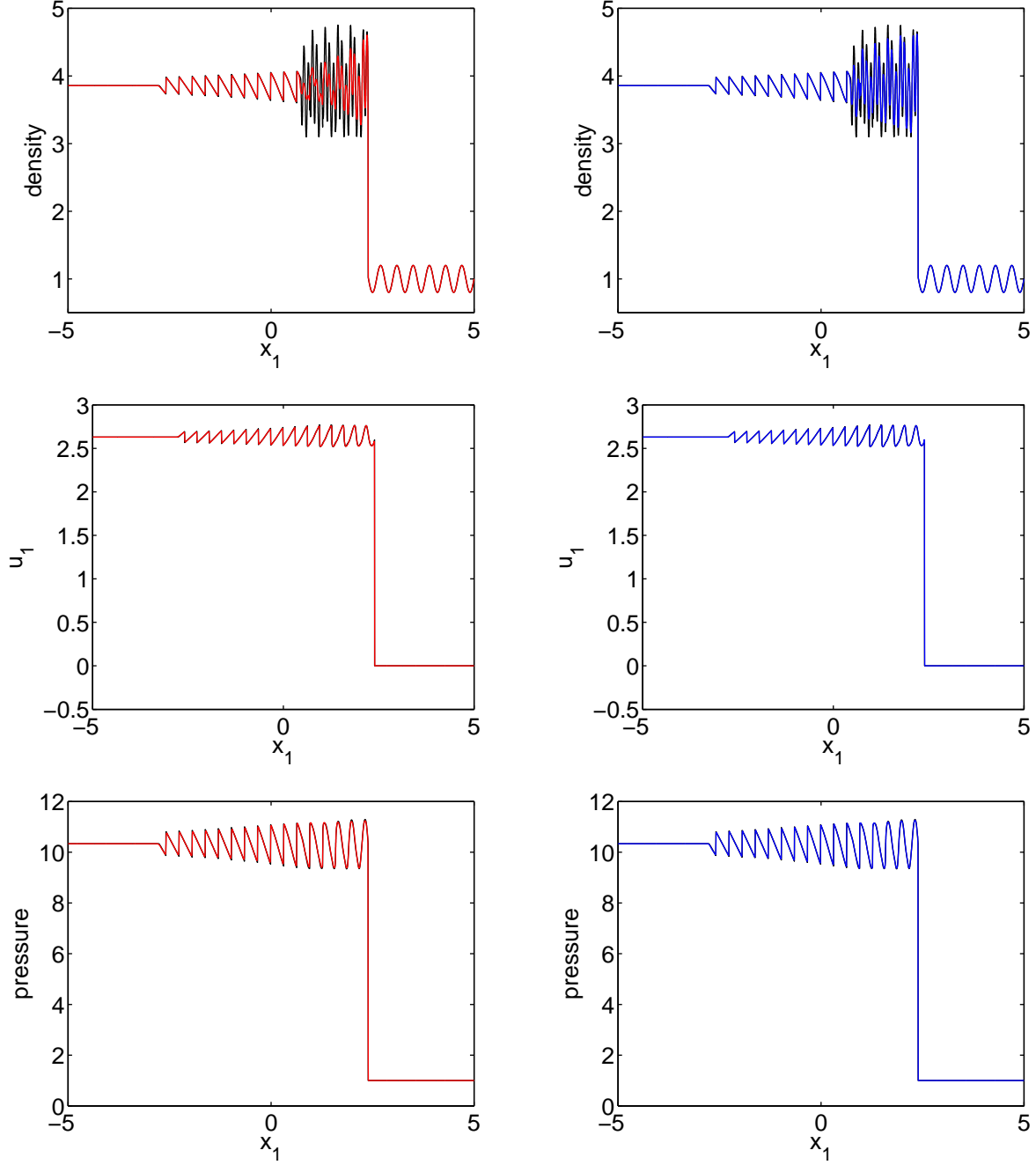
Fig. 8. Comparison of the numerical approximations at $t = 1.8$ for the Shu-Osher test problem and $m = 16$. For both images the black line represents the reference solution while the red line (left) shows the Godunov approximation and the blue line (right) shows the FCT approximation. From top to bottom are density, velocity, and pressure. (For interpretation of the references to color in this figure legend, the reader is referred to the web version of this article)

is a measure of grid size. Here $\mathcal{A}$ and $\mathcal{R}$ are defined as

$$\mathcal{R}([x_{1,a}, x_{1,b}] \times [x_{2,a}, x_{2,b}], N_1, N_2) = \big\{ (x_{1,a} + i_1 \Delta x_1, \, x_{2,a} + i_2 \Delta x_2) \,|$$

$$\Delta x_k = (x_{k,b} - x_{k,a})/N_k, \, i_k = 0, 1, \ldots, N_k, \, k = 1, 2 \big\}.$$
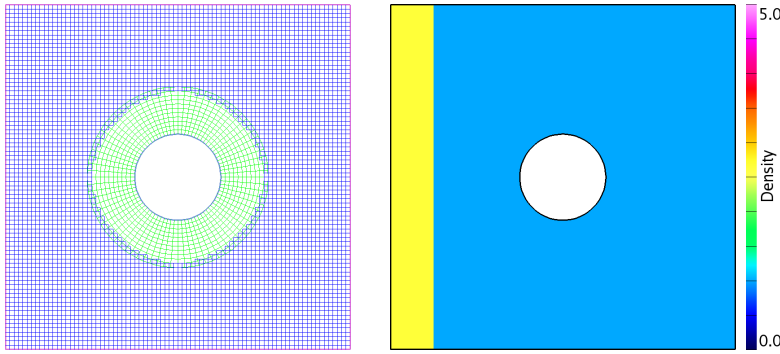
Fig. 9. Overlapping grid structure (left) and color contour of the initial density (right). The overlapping grid structure which is used to capture geometry and in general this structure will have additional adaptive mesh refinement grids to locally increase resolution. The initial density shows a $M = 2.0$ shock in air (ideal gas with $\gamma = 1.4$) moving from left to right. (For interpretation of the references to color in this figure legend, the reader is referred to the web version of this article)

and

$$\mathcal{A}\left((x_{1,c}, x_{2,c}), [r_a, r_b], N_r, N_\theta\right) = \left\{(x_{1,c}, x_{2,c}) + r_{i_r}(\cos(\theta_{i_\theta}), \sin(\theta_{i_\theta})) \mid \right.$$

$$\left. r_{i_r} = r_a + i_r(r_b - r_a)/N_r, \ \theta_{i_\theta} = 2\pi i_\theta/N_\theta, \ i_k = 0, 1, \ldots, N_k, \ k = r, \theta\right\}.$$

The boundary around the cylinder is defined as a slip wall (see [17]), the left boundary as an inflow, and the remaining boundaries are given outflow conditions. Interactions of interest are limited to those associated with the shock/cylinder interaction and provided that the simulation is not run too far in time, waves generated at the cylinder are unable to reach the exterior boundaries. As such the exterior boundary condition choice has no influence and is made for convenience. Figure 9 shows the computational mesh as well as color contours of density for the initial conditions. Numerical values for the initial conditions in primitive quantities, corresponding to a Mach 2 shock in air ($\gamma = 1.4$), were shown previously in Table 5.

The comparisons carried out in this paper use the resolution displayed in Figure 9 and discussed above as the coarsest simulation. Adaptive mesh refinement (AMR) is then used for successive resolutions. For this test of shock interaction with a single cylinder, each additional level of AMR uses a factor four refinement in each coordinate direction and so the four resolutions investigated have approximate grid spacings $h \approx 0.05$, 0.0125, 0.003124, and 0.00078125. Notice that because the initial condition uses a perfect jump, there exists numerical artifacts along the c^- characteristic and contact path. No effort is made to remove these and their contribution may be seen throughout the simulations.

Figure 10 shows the computed density using both methods for $t = 0.6$, $t = 1.0$, and $t = 1.4$ as the incident shock reflects from the cylinder boundary. Particularly at the earlier times, one would be hard pressed to identify differences between the approximations from these images, much less determine if one method was behaving better in any way. For $t = 1.4$ however, there are clear differences, particularly in the regions where vorticity is being generated downwind of the cylinder. In these regions, it seems that the FCT method contains more structures as well as more noise, but it is not at all clear if these additional structures have physical meaning. To give a better indication of what is happening, Figure 11 shows the AMR grid structure, numerical Schlieren images, and the computed pressure at $t = 1.4$. The numerical Schlieren image is a gray-scale image of

$$\sigma = \exp\left\{-\beta\left(\frac{|\nabla\rho| - \min|\nabla\rho|}{\max|\nabla\rho| - \min|\nabla\rho|}\right)\right\},$$

where the minimum and maximum are taken over the entire domain, and β is the exposure (taken to be 15). The range of σ plotted is 0.4 to 1 where the lower limit is assigned to black and the upper limit is assigned to white in the gray-scale image.

The image of the AMR grids is perhaps the most informative because it demonstrates the increased noise created by the FCT method. Numerical noise tends to flag cells for refinement by the AMR algorithm and so a
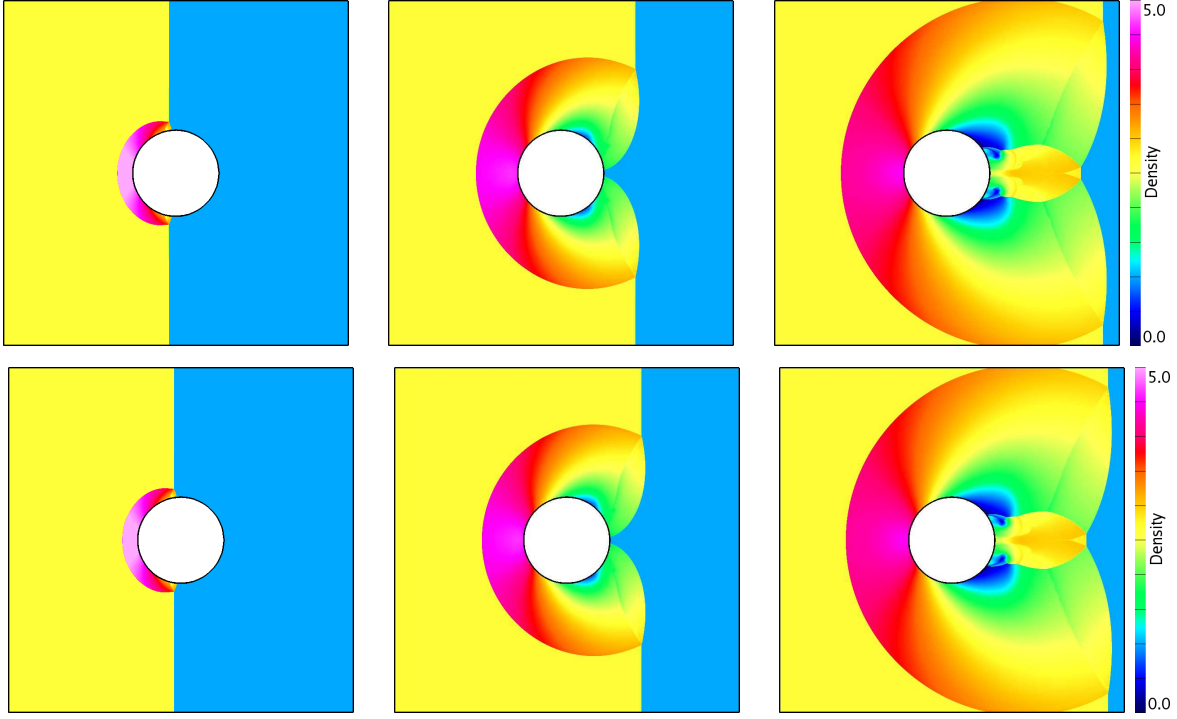
Fig. 10. Color contours of density for the finest resolution using FCT (top) and Godunov's method (bottom) at $t = 0.6$ (left), $t = 1.0$ (middle), and $t = 1.4$ (right). (For interpretation of the references to color in this figure legend, the reader is referred to the web version of this article)
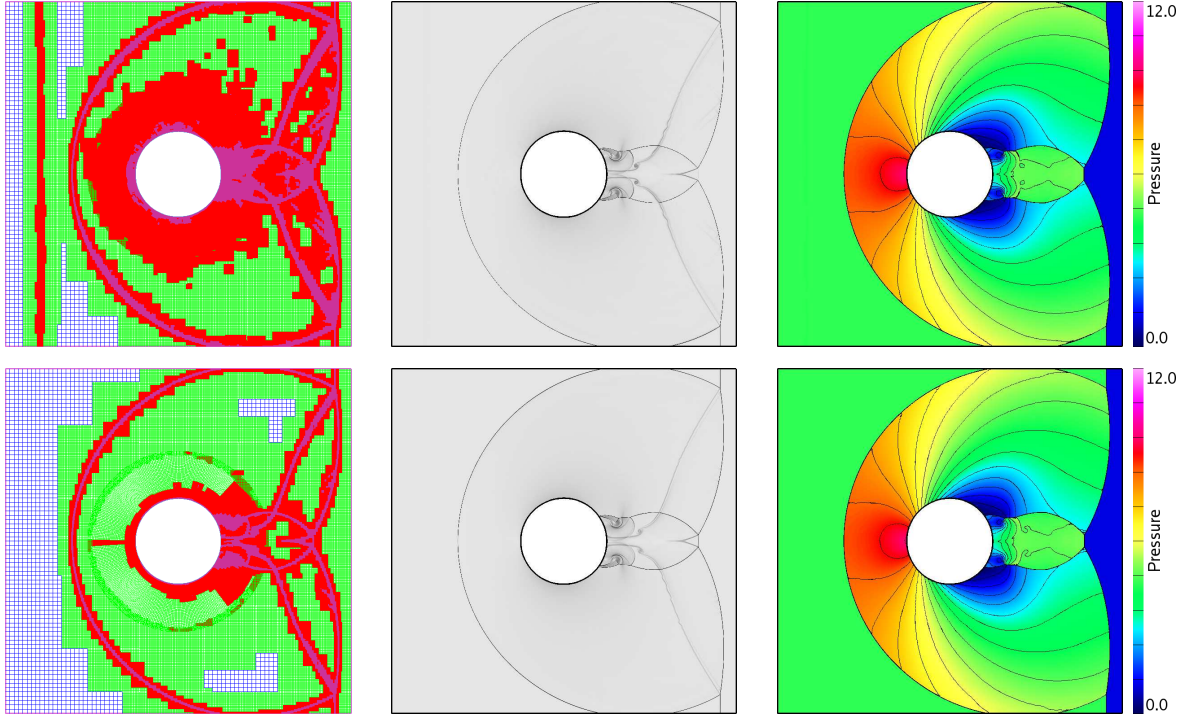

Fig. 11. AMR grid structure (left), numerical Schlieren images (center) and pressure (right) for the FCT method (top) and Godunov's method (bottom) for the finest resolution simulation at $t = 1.4$. Included in the pressure plots are 21 equally spaced contour lines so that one may more accurately judge discrepancies in the flow fields for the two methods. (For interpretation of the references to color in this figure legend, the reader is referred to the web version of this article)
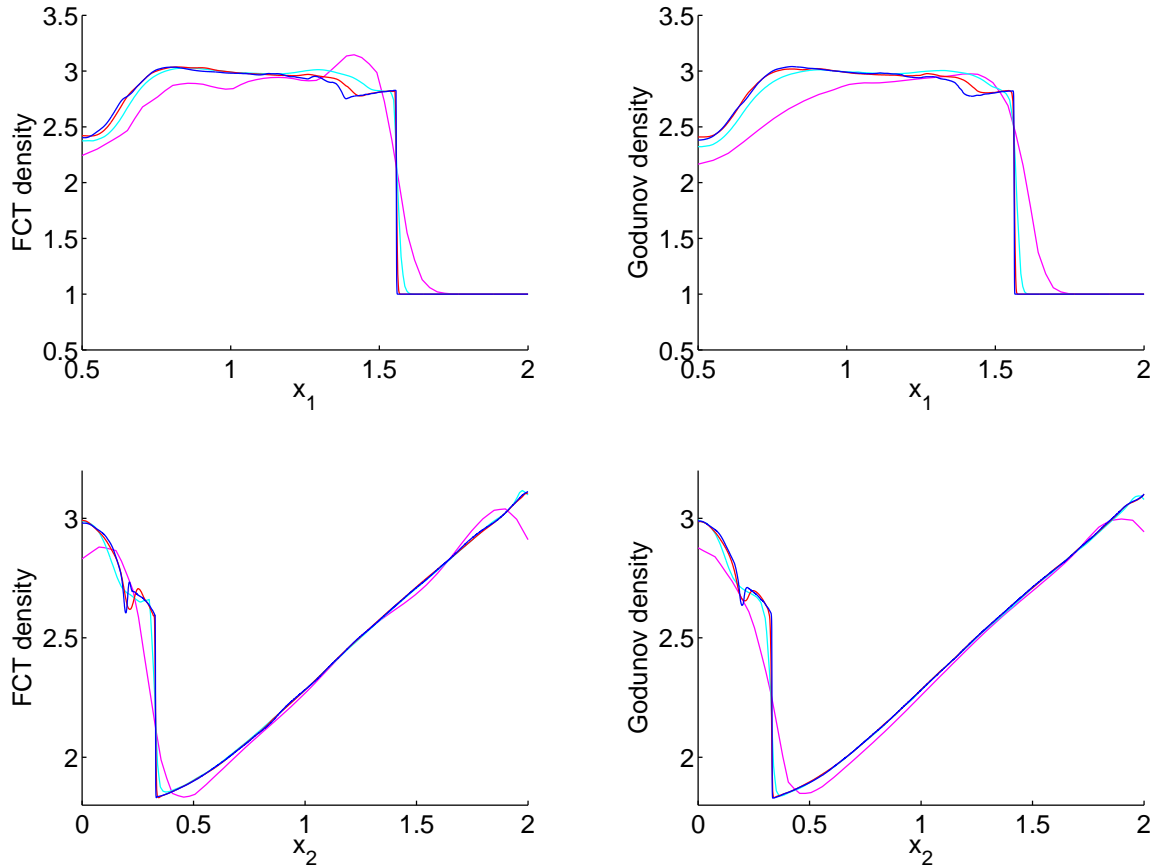
Fig. 12. Solution convergence along the lines $x_2 = 0$ (top) and $x_1 = 1$ (bottom) for the FCT method (left) and the Godunov method (right) on the shock-cylinder problem. Shown here is the density with the colors indicating numerical resolution. Maroon represents the solution with no AMR while cyan, red, and finally blue represent 1, 2, and 3 levels of additional factor four adaptive meshes respectively. (For interpretation of the references to color in this figure legend, the reader is referred to the web version of this article)

larger portion of the domain is covered by fine meshes for the FCT simulation. This type of noise, also interpretable as staircases, is a common phenomenon in FCT simulations. There are ways to alleviate this problem, such as higher levels of artificial diffusion, alternate high order fluxes, and others, but such changes alter the overall performance of the FCT method. Furthermore, in our experience, there is no single method which eliminates the high frequency noise production from the FCT method for all simulations. For the FCT implementation used here, Figure 11 demonstrates a typical result when highly-resolved simulations are considered. In contrast, the Godunov approximation shows no sign of this type of high frequency noise and the AMR meshes conform closely to the locations of rapid change, such as shocks and contacts. It is worth noting that the remnant of the initial condition on the c^- characteristic has flagged refinement for the FCT solution whereas it is almost entirely gone for the Godunov solution. Finally notice the increased presence of Kelvin-Helmholtz roll-ups along the slip line for the FCT approximation as seen in the Schlieren image. Although both approximations contain this feature, and increased resolution will bring this out further, the FCT approximation is developing them to a larger degree at this fixed resolution. This again is evidence of smaller artificial dissipation for the FCT method.

A quantitative analysis of convergence behavior for this problem is now presented using a similar method to that used in Section 4.4. Figure 12 shows line plots of the approximations along the lines $x_2 = 0$ with $x_1 \in [0.5, 2.0]$ and $x_1 = 1$ with $x_2 \in [0, 2]$. In this figure, the solution for each method at each resolution is displayed. From these plots one can again see the trend that FCT captures features more sharply, but that those approximations contain more noise. To contrast this, the Godunov approximations are generally smoother and slightly more smeared. Also one can see that both schemes appear to be self convergent and a more quantitative analysis shows this to be the

case. To perform such an analysis, the solution in Figure 12 is interpolated to second order onto a uniform mesh along each line and a self convergence study performed using the discrete L_1 norm. The reference solution is taken to be the finest resolution. These results are shown in tables 11 through 12. Here it is seen that while the FCT

m	$e_\rho(m)$ F	$e_\rho(m)$ G	$e_{u_1}(m)$ F	$e_{u_1}(m)$ G	$e_{u_2}(m)$ F	$e_{u_2}(m)$ G	$e_p(m)$ F	$e_p(m)$ G
1	2.18e−1	2.68e−1	1.61e−1	1.90e−1	7.84e−3	6.38e−3	2.67e−1	3.46e−1
4	6.81e−2	7.51e−2	8.06e−2	8.00e−2	5.14e−3	7.91e−3	7.59e−2	7.26e−2
16	2.23e−2	2.24e−2	3.11e−2	3.04e−2	3.12e−3	4.62e−3	3.58e−2	3.02e−2
κ	0.82	0.90	0.59	0.66	0.33	0.12	0.72	0.88

Table 11
Self convergence for the FCT (F) and Godunov (G) schemes along the line $x_2 = 0$ along with least squares fit for the convergence rate κ for the shock-cylinder problem. Here m measures effective grid resolution with mesh spacing $h \approx \frac{1}{40m}$.

m	$e_\rho(m)$ F	$e_\rho(m)$ G	$e_{u_1}(m)$ F	$e_{u_1}(m)$ G	$e_{u_2}(m)$ F	$e_{u_2}(m)$ G	$e_p(m)$ F	$e_p(m)$ G
1	7.07e−2	8.12e−2	1.25e−2	2.85e−2	4.09e−2	5.05e−2	1.23e−1	1.23e−1
4	2.13e−2	1.93e−2	7.70e−3	8.34e−3	1.41e−2	1.66e−2	3.08e−2	3.54e−2
16	9.46e−3	8.17e−3	4.73e−3	7.64e−3	9.48e−2	9.00e−3	1.36e−2	1.48e−2
κ	0.73	0.83	0.35	0.47	0.53	0.62	0.79	0.76

Table 12
Self convergence for the FCT (F) and Godunov (G) schemes along the line $x_1 = 1$ along with least squares fit for the convergence rate κ for the shock-cylinder problem. Here m measures effective grid resolution with mesh spacing $h \approx \frac{1}{40m}$.

method does seem to be able to capture features more sharply for a given resolution, the smoother simulation results produced by the Godunov method cause generally higher convergence rates for these more complex flows. It is also interesting to see that convergence results for all quantities, including the velocities and pressure which do not jump through a contact wave, see sub-linear convergence despite the high resolution of the simulations. On possible explanation for this behavior is that sub-linear convergence of the density near contacts is driving the convergence rates of all quantities. This might occur, for example, through the interaction of non-linear shock and rarefaction waves with a captured contact discontinuity at degraded accuracy.

4.6 Irregular Mach Reflection of a Strong Shock

The final test considered in this paper is that of irregular Mach reflection of a strong shock at an inclined ramp. This classic example has been investigated by many authors [27,36,23] as well as demonstrated experimentally [37]. In this problem, a Mach 10 shock impacts a ramp which is inclined 30° from the normal shock propagation direction. The result is a complex interaction known as irregular Mach reflection. Numerically, this flow can cause a carbuncle like instability [38,39] for some numerical methods if proper care is not taken.

Traditionally this test problem has been solved by inclining the incident shock to a Cartesian grid and using special boundary conditions to simulate the transition region at the start of the ramp. For the simulations presented in this paper, the geometry of a 30° ramp is realized using overlapping grids and then a Mach 10 shock is impacted onto this ramp. The geometry we consider consists of a thin boundary fitted portion to model the ramp in union with a background Cartesian grid for the remaining bulk of the computational domain. The
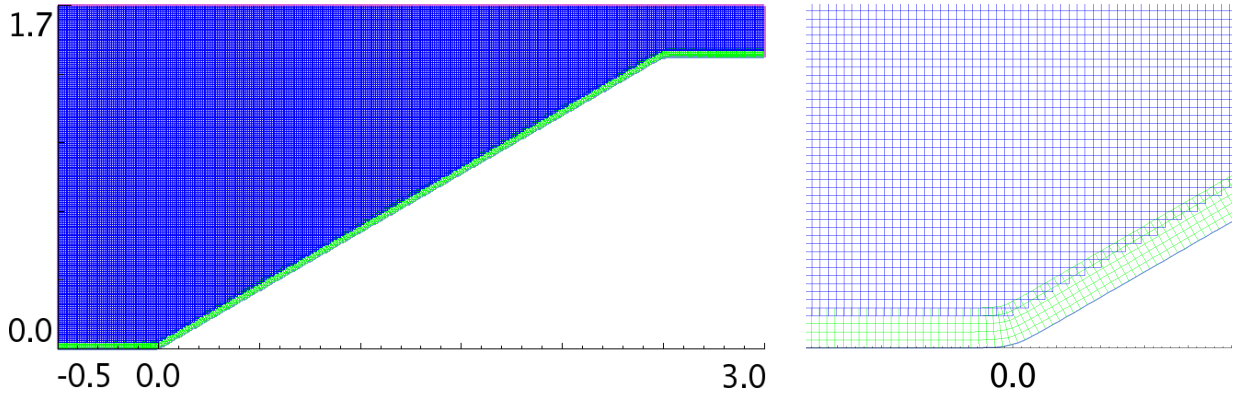
Fig. 13. Basic overlapping grid used for the simulation of irregular Mach reflection on an inclined ramp. The boundary fitted ramp grid is seen in green and the background Cartesian mesh in blue. The full geometry (left) shows what looks like sharp transitions to represent the ramp corners, but the zoom near the origin (right) shows that these corners are very slightly rounded. (For interpretation of the references to color in this figure legend, the reader is referred to the web version of this article)

background Cartesian mesh is defined by $\mathcal{R}([-0.5, 3.0] \times [0, 1.7], 420, 340)$. Although the boundary fitted portion does not lend itself to such a simple mathematical expression, a verbal description will suffice for our purpopses. The boundary of this ramp grid defines a smooth transition from the line $x_2 = 0$ to the line $x_2 = x_1/\sqrt{3}$, and finally to the line $x_2 = 1.4438$. These transitions are defined in terms of integrals of hyperbolic tangent functions and are therefore smooth [40]. The ramp grid extends along normals into the domain and the mesh spacing is chosen to approximately match that of the background Cartesian grid. The basic mesh is shown in Figure 13 where both the full geometry and a zoom near the origin, the ramp initiation, are shown. At the scale of the full geometry it is difficult to see the rounding of the corners, but the close up image makes this rounding clear. A rounded corner will have some effect on the solution as it compares to a perfectly sharp corner, but such effects effect have been studied for example in [41,16] and found to be of little consequence for such flows when the radius of curvature is small as compared to the flow features of interest (as is the case here).

Initial conditions for the planar shock are found with reference to [35] for a $\gamma = 1.4$ ideal gas and those values are given in Table 13. The initial shock is located at $x_1 = -0.25$ (for reference the left-most boundary is $x_1 = -0.5$ and the ramp incline begins at $x_1 = 0$) and time integration is performed to $t = 0.2$. Boundary conditions are set using a slip wall condition along the ramp boundary and outflow conditions elsewhere. For these simulations, the base mesh has roughly equal mesh spacing throughout the domain with $h \approx \frac{1}{120}$. Simulations are performed at four resolutions starting with only the base mesh and then progressing through to use one additional level of factor four refinement, two additional levels of factor three refinement, and finally two additional levels of factor four refinement.

	ρ	u_1	u_2	p
pre-shock	1.4	0.0	0.0	1.0
post-shock	8.0	8.25	0.0	11.65

Table 13
Pre- and post-shock states for a Mach 10 planar shock.

Figure 14 shows the approximations obtained using the FCT and Godunov methods at the finest resolution which yields approximate mesh spacing $h \approx 5.21 \times 10^{-4}$. At this scale there are some apparent differences that merit mention. First notice the increased noise production by the FCT method as shown by the increased proportion of the domain flagged for AMR refinement. Notice that both simulations retain remnants of the initial condition along the c^- characteristic and contact path. For both cases, these remnants are covered with fine AMR meshes, although the refinement for the FCT algorithm covers a larger region. Also it is seen that the minimum pressure
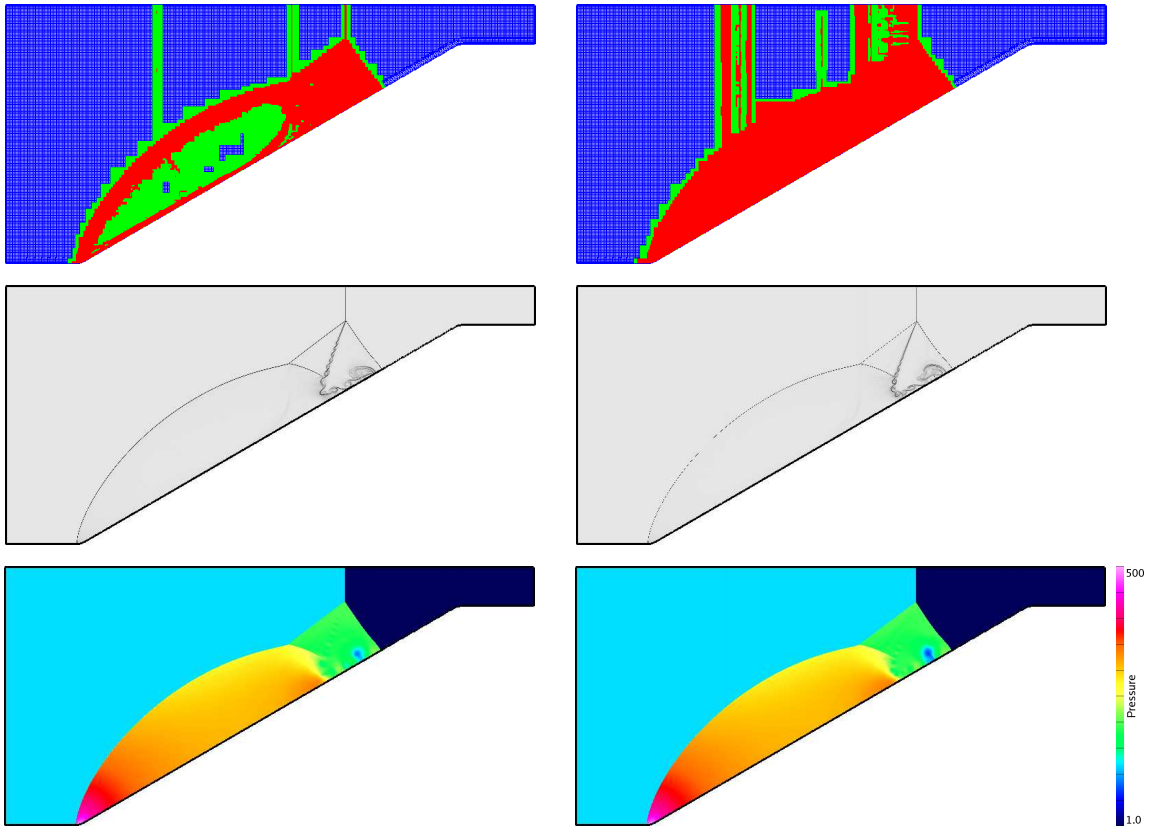
24

Fig. 14. Simulation results at $t = 0.2$ for the Godunov method (left) and FCT (right) with 3 levels of factor 4 refinement. Shown are the AMR mesh (top), a numerical Schlieren image (middle), and pressure (bottom). Notice the increase in noise produced by the FCT method as evidenced by the larger region flagged for AMR refinement. Also notice the lower pressure achieved by the FCT method within the main vortex. (For interpretation of the references to color in this figure legend, the reader is referred to the web version of this article)

inside the main vortex is lower for the FCT simulation than for Godunov.

In order to gain more insight about what is happening near the main vortex, Figure 15 shows close-up numerical Schlieren images near that structure. All resolutions are displayed so that the effect of mesh resolution can be seen. For both simulation techniques, the main vortex is poorly captured at low resolutions but with increasing mesh resolution the main features begin develop. The roll-ups along the slip sheets become pronounced for both methods with the Godunov solution showing more detailed structure. The main point here centers on the final two resolutions where the main vortex becomes well formed. Notice that for the Godunov method the main vortex remains as a coherent single vortical structure, while for the FCT method the vortex begins to break down and show more complex behavior. Comparing this behavior with what is seen in [23] shows that the Godunov methods (for [23] the PPM method) tend to maintain a coherent single structure, while the other methods (the hybrid WENO method in [23] and FCT here) produce a vortex which begins to loose coherence at very high resolution. This type of behavior calls into question the limit processes of the various schemes and wether the various methods are in fact approaching the same vanishing viscosity solution. This is an interesting question and will be the subject of future work.

In [23], the strength of the central vortex is judged by plotting the lowest pressure and density from the main vortex as functions of mesh resolution. The fact that this central vortex seems to have fundamentally different behavior for the different methods indicates that a direct measure of peak vorticity may be a more accurate indicator of vortex strength. Figure 16 plots both the minimum temperature, defined as p/ρ, as well as a direct computation of peak vorticity as functions of mesh resolution. These plots reveal that both schemes reduce the minimum vortex temperature, but that temperature reduces more rapidly for the FCT approximations. On the other hand, the maximum vorticity is seen to increase at a greater rate for the Godunov solution.
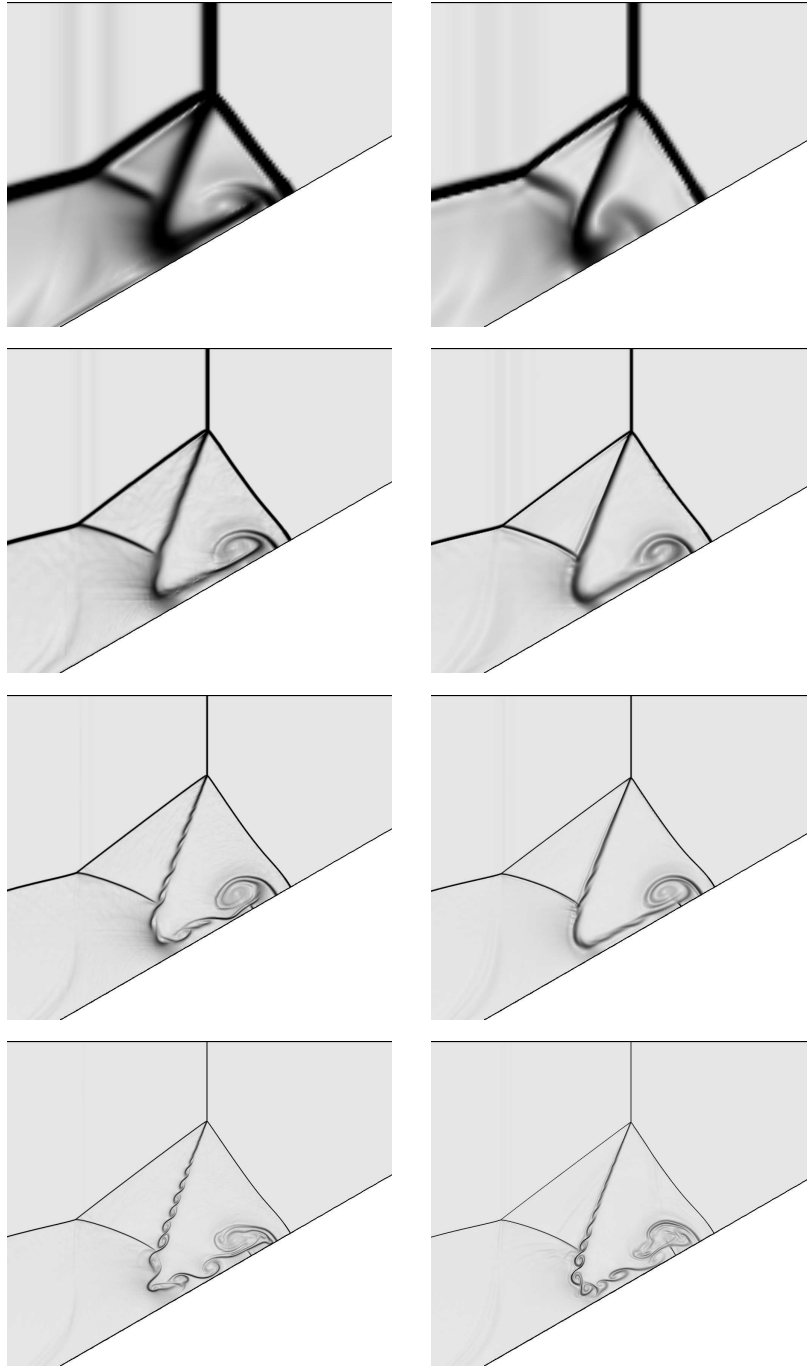
Fig. 15. Zoom of the numerical Schlieren images near the triple point and main vortex for Godunov (left) and FCT (right). Resolution increases from top to bottom with approximate grid spacings $h \approx 1/120$, $1/480$, $1/1080$, and $1/1920$ respectively. Notice the loss of coherence of the main vortex for the FCT method at the highest resolutions.

To perform a convergence study for this flow, the simulation data along the ramp boundary is extracted. Figure 17 plots the density along these lines as a function of ramp distance for all resolutions of the FCT and Godunov simulations. Discrete L_1 errors are then computed with reference to the finest simulation and the convergence character computed in a least squares sense. Table 14 shows the computed errors and the least squares convergence rates for primitive quantities along the ramp using both methods. The fist thing to notice in these tables is that for the Godunov method, the computed error in the velocities has increased as the resolution increased from $1/480$ to $1/1080$ despite the fact that least squares convergence is exhibited at the relatively high rate of .41. Notice also that this happens while the convergence character for density and pressure are relatively
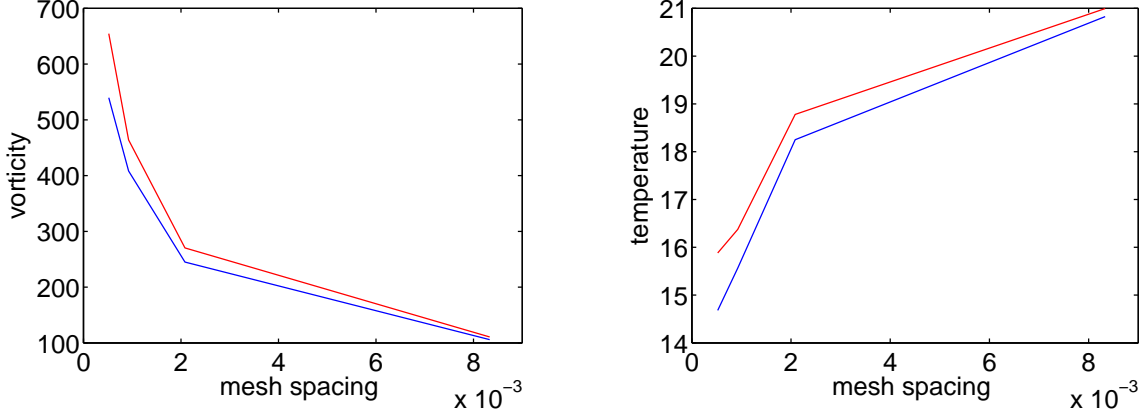
Fig. 16. Maximum vorticity within the main vortex as a function of mesh spacing (left) and minimum temperature, defined as p/ρ, as a function of mesh spacing (right). Here the red line on top for both plots reflects the Godunov method and the blue line represents FCT. Here the main vortex continually increases in strength for both simulations as the mesh is refined. (For interpretation of the references to color in this figure legend, the reader is referred to the web version of this article)
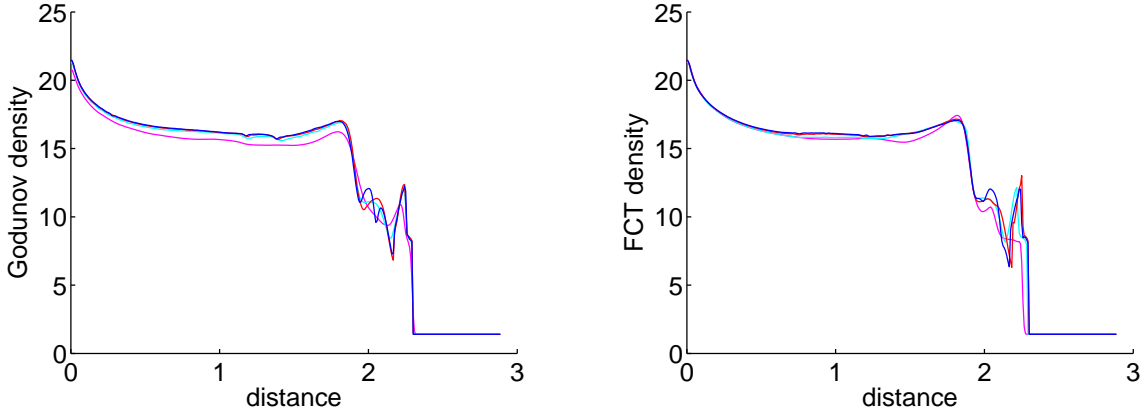

Fig. 17. Line plot of density along the ramp as a function of distance from the start of the ramp for Godunov (left) and FCT (right). Increasing resolutions are represented by maroon, cyan, red, and blue. (For interpretation of the references to color in this figure legend, the reader is referred to the web version of this article)

m	$e_\rho(m)$ F	$e_\rho(m)$ G	$e_{u_1}(m)$ F	$e_{u_1}(m)$ G	$e_{u_2}(m)$ F	$e_{u_2}(m)$ G	$e_p(m)$ F	$e_p(m)$ G
1	1.23e0	1.61e0	1.46e0	5.42e−1	8.43e−1	3.13e−1	2.33e1	1.24e1
4	6.39e−1	4.67e−1	4.02e−1	2.18e−1	2.32e−1	1.26e−1	1.17e1	8.80e0
9	3.49e−1	2.90e−1	2.83e−1	2.36e−1	1.63e−1	1.36e−1	5.68e0	5.74e0
κ	0.56	0.79	0.77	0.41	0.77	0.41	0.63	0.34

Table 14
Self convergence for the FCT (F) and Godunov (G) schemes along the ramp as well as least squares fit for the convergence rate κ. Here m measures effective grid resolution with mesh spacing $h \approx \frac{1}{120m}$.

good but nowhere near first order. By contrast, the FCT scheme is demonstrated to be consistently converging for all quantities even up to the finest resolution simulations. Such results are valuable, but should not be taken out of context. The underlying flow is complex and is characterized by unstable features, such as Kelvin-Helmholtz roll-ups. Numerical simulations of such unstable features are likely to produce strange convergence character and

perhaps not to converge at all.

5 Qualitative Comments About Timings

As previously mentioned one aim of this study is to provide a reasonably detailed comparison of an FCT implementation with a implementation of a high-resolution Godunov method. In this assessment, a quantitative comparison of these techniques has included convergence (oder-of-accuracy) results as well as details concerning the relative accuracy of the methods on a set of test problems. One critical aspect that has been neglected is the time required to obtain simulation results for the different solution methods studied in this paper. This question has not been addressed for the very specific reason that the Godunov code used here is mature and has been through years of optimization. The FCT code however, has been recently developed for the purposes of this study and has not been through the same optimization process. However, we do believe that some qualitative remarks about issues related to efficiency are in order.

First, as implemented, the FCT method requires approximately a factor of 10 more computational time to advance the solution one time step for a given mesh. In part this is due to non-optimal implementation but a large part is due to the FCT algorithm being more costly than the Godunov method. One major differences, at least in the present implementation are that the FCT code requires one linearization for each cell face as opposed to one per direction per cell for Godunov's method. Each linearization in the FCT code requires that a large number of quantities be transformed as compared to Godunov's method. Furthermore, the FCT stencil is 7 points rather than 5 for Godunov's method. A conservative estimate based on our experience is that FCT might be perhaps five times slower than Godunov for a given mesh and two equally mature implementations.

Another important concern is the increased high-frequency noise generated in the FCT solutions. Such noise results in larger regions of the flow for which fine AMR meshes are required. For example, the finest resolution computations of irregular Mach reflection in Section 4.6 have the FCT approximation containing 1.8 times as many grid cells as the Godunov method at the final time. Assuming the majority of the cells reside on the finest level of refinement, a relatively accurate assumption here, 1.8 times the number of cells results in roughly 1.8 times the computational cost. Furthermore, the necessity to include fourth order diffusion for FCT, also an artifact of increased noise production, results in a commensurate reduction in the time step size in order to satisfy the stability constraint. Also recall that the CFL limit for monotonicity in the FCT method is 0.5 so these simulations in this paper were run at a CFL of 0.4 while the Godunov results were obtained at CFL 0.9. Taking the ramp computations as an example, the end result was approximately a factor of 2.8 reduction in time step size for FCT as compared to Godunov. Despite the inefficient implementation of FCT used for this work, it is fair to say that the FCT is a costly algorithm when compared to Godunov. For every case presented here, a simulation at substantially higher resolution, and commensurately smaller error, can be obtained by the Godunov method for a given amount of wall clock time. This is expected to remain true even for an efficient implementation of this FCT algorithm.

We believe these comments on timings are important to make despite their somewhat qualitative nature. Primarily this is so that anyone wishing to adopt our implementation, or one similar to it, understands the computational expense associated with it. Of course there are ideas that could be considered to help reduce the high cost and an efficient implementation would be a reasonable place to start. There are also potential ways to help reduce the levels of high frequency noise generated by this particular FCT method. These might include the development of stronger higher order dissipation to add more effective levels of numerical dissipation to control the generation of noise. However, this would be difficult to automate for general use and would tend to negate the increased resolving power of the underlying technique. Another approach might be to use an alternate high-order method rather than the centered stencil. Our preliminary studies using the second order unlimited Godunov flux indicate that this does reduce the production of high-frequency noise, but the gains are limited when very high resolutions are attained. Finally it is possible that the basic approach might be modified along the lines discussed by Kuzmin to develop TVD-like methods [6] that tend to introduce less high frequency noise.

6   Conclusions

This paper has outlined the development of a high-resolution FCT algorithm for the Euler equations on structured overlapping meshes. The development and implementation of the FCT method for overlapping meshes was based on the Overture framework and included modifications and extensions to the usual FCT algorithm. Such extensions included the obvious modifications required for operation with mapped overlapping meshes as well as the inclusion of a Jameson style artificial viscosity to remove noise produced by FCT. Improvements were made to the FCT algorithm to fix the appearance of entropy violating shocks that can occur at sonic points in rarefaction waves. Difficulties that appear in strong rarefaction waves where the gas separates at greater than the sonic velocities and produces a near vacuum state were also addressed.

The efficacy of our new FCT method was then demonstrated on a set of benchmark high-speed compressible flow problems. This investigation confirmed the appropriate convergence character for isolated contact and shock waves. The contact case also established, for the first time, that the FCT method is in fact a non-compressive limiting strategy. Comparison of the computed results with a Godunov scheme also provides some context concerning the performance of FCT as it relates to other high-resolution techniques. More complex flows in two dimensions demonstrated the overlapping mesh capabilities and again a comparison to the Godunov scheme helps to elucidate the strengths and weaknesses of such an FCT approach. Results were presented for the interaction of a shock wave with a rigid immobile cylinder, and a problem of the irregular Mach reflection of a strong shock on an inclined ramp. All of these tests serve to verify the robust nature of the FCT solver as well as to demonstrate the efficacy of the overall implementation. It is also seen that the solution approximations produced by the FCT method are generally marginally more accurate than those produced by the Godunov method, but that the cost of increased accuracy significant. Further work is required to provide a quantitative assessment concerning issues of efficiency. However, the firm comparison presented here give assurance that the FCT method may be a viable option for cases where Riemann solutions are not possible, or for unstructured meshes where a Godunov type method may not be easily implemented.

References

[1] J. P. Boris, D. L. Book, Flux-corrected transport. I. SHASTA, a fluid transport algorithm that works, J. Comput. Phys. 11 (1973) 38–69.

[2] J. P. Boris, D. L. Book, K. Hain, Flux-corrected transport II: Generalizations of the method, J. Comput. Phys. 18 (1975) 248–283.

[3] J. P. Boris, D. L. Book, Flux-corrected transport III. Minimal-error FCT algorithms, J. Comput. Phys. 20 (1976) 397–431.

[4] C. Richard DeVore, Flux-corrected transport techniques for multidimensional compressible magnetohydrodynamics, J. Comput. Phys. 92 (1991) 142–160.

[5] G. Tóth, D. Odstrcil, Comparison of some flux corrected transport and total variation diminishing numerical schemes for hydrodynamic and magnetohydrodynamic problems, J. Comput. Phys. 128 (1) (1996) 82–100.

[6] D. Kuzmin, R. Löhner, S. Turek (Eds.), Flux-Corrected Transport, Springer, 2005.

[7] G.-S. Jiang, C.-W. Shu, Efficient implementation of weighted eno schemes, J. Comput. Phys. 126 (1) (1996) 202–228.

[8] D. S. Balsara, C.-W. Shu, Monotonicity preserving weighted essentially non-oscillatory schemes with increasingly high order of accuracy, J. Comput. Phys. 160 (2) (2000) 405–452.

[9] A. Harten, B. Engquist, S. Osher, S. Chakravarthy, Uniformly high order accurate essentially non-oscillitory schemes, III, J. Comput. Phys. 71 (1987) 231–303.

[10] C.-W. Shu, S. Osher, Efficient implementation of essentially non-oscillatory shock-capturing schemes, J. Comput. Phys. 77 (2) (1988) 439–471.

[11] C.-W. Shu, S. Osher, Efficient implementation of essentially non-oscillatory shock-capturing schemes, II, J. Comput. Phys. 83 (1) (1989) 32–78.

[12] A. Harten, P. D. Lax, B. van Leer, On upstream differencing and Godunov type schemes for hyperbolic conservation laws, SIAM Rev. 25 (1983) 33–61.

[13] P. Colella, P. R. Woodward, The piecewise parabolic method (PPM) for gas-dynamical simulations, J. Comput. Phys. 54 (1) (1984) 174–201.

[14] E. F. Toro, Riemann Solvers and Numerical Methods for Fluid Dynamics, Springer, Berlin, 1999.

[15] G. Chesshire, W. Henshaw, Composite overlapping meshes for the solution of partial differential equations, J. Comput. Phys. 90 (1990) 1–64.

[16] W. D. Henshaw, D. W. Schwendeman, An adaptive numerical scheme for high-speed reactive flow on overlapping grids, J. Comput. Phys. 191 (2) (2003) 420–447.

[17] W. D. Henshaw, D. W. Schwendeman, Moving overlapping grids with adaptive mesh refinement for high-speed flow, J. Comput. Phys. 216 (2) (2006) 744–779.

[18] J. W. Banks, D. W. Schwendeman, A. K. Kapila, W. D. Henshaw, A high-resolution Godunov method for compressible multi-material flow on overlapping grids, J. Comput. Phys. 223 (2007) 262–297.

[19] T. Baker, Mesh generation for the computation of flowfields over complex aerodynamic shapes, Computers Math. Applic. 24 (1992) 103–127.

[20] W. Chan, A unified overset grid generation graphical interface and new concepts on automatic gridding around surface discontinuities, in: Proceedings of the 4th Symposium on Overset Composite Grid and Solution Technology, 1998.

[21] N. A. Petersson, Hole-cutting for three-dimensional overlapping grids, SIAM J. Sci. Comp. 21 (1999) 646–665.

[22] J. A. Greenough, W. J. Rider, A quantitative comparison of numerical methods for the compressible euler equations: fifth-order WENO and piecewise-linear godunov, J. Comput. Phys. 196 (2004) 259–281.

[23] W. J. Rider, J. A. Greenough, J. R. Kamm, Accurate monotonicity- and extrema-preserving methods through adaptive nonlinear hybridizations, J. Comput. Phys. 225 (2007) 1827–1848.

[24] W. D. Henshaw, OverBlown: A fluid flow solver for overlapping grids, reference guide, Research Report UCRL-MA-134289, Lawrence Livermore National Laboratory (1999).

[25] M. J. Berger, J. Oliger, Adaptive mesh refinemenr for hyperbolic partial differential equations, J. Comput. Phys. 53 (1984) 484–512.

[26] S. T. Zalesak, Fully multidimensional flux-corrected transport algorithms for fluids, J. Comput. Phys. 31 (1979) 335–362.

[27] S. T. Zalesak, The design of flux-corrected transport (FCT) algorithms on structured grids, Ph.D. thesis, George Mason University (2005).

[28] U. M. Ascher, L. R. Petzold, Computer Methods for Ordinary Differential Equations and Differential-Algebraic Equations, SIAM, Philadelphia, 1998.

[29] A. Jameson, W. Schmidt, E. Turkel, Numerical solution of the euler equations by finite volume methods using runge-kutta time-stepping schemes, in: AIAA 14th Fluid and Plasma Dynamic Conference, 1981.

[30] A. Jameson, Transonic flow calculations for aircraft, in: Numerical Methods in Fluid Dynamics, vol. 1127 of Lecture Notes in Mathematics, Springer-Verlag, 1983, pp. 156–242.

[31] G. A. Sod, A survey of several finite difference methods for systems of nonlinear hyperbolic conservation laws, J. Comput. Phys. 27 (1) (1978) 1–31.

[32] G. W. Hedstrom, The rate of convergence of some difference schemes, J. SIAM Numer. Anal. 5 (2) (1968) 363–406.

[33] A. Harten, The artificial compression method for computation of shocks and contact discontinuities. I. single conservation laws, Commun. Pur. Appl. Math. 30 (5) (1977) 611–638.

[34] J. W. Banks, T. Aslam, W. J. Rider, On sub-linear convergence for linearly degenerate waves in capturing schemes, J. Comput. Phys. 227 (14) (2008) 6985–7002.

[35] G. B. Whitham, Linear and Nonlinear Waves, Wiley-Interscience, New York, 1974.

[36] P. Woodward, P. Colella, The numerical simulation of two-dimensional fluid flow with strong shocks, J. Comput. Phys. 54 (1984) 115–173.

[37] M. V. Dyke, An Album of Fluid Motion, The Parabolic Press, Stanford, California, 1982.

[38] J. J. Quirk, A contribution to the great riemann solver debate, Int. J. Numer. Meth. Fl. 18 (1994) 555–574.

[39] M. Dumbser, J.-M. Moschetta, J. Gressier, A matrix stability analysis of the carbuncle phenomenon, J. Comput. Phys. 197 (2004) 647–670.

[40] W. Henshaw, Mappings for Overture, a description of the Mapping class and documentation for many useful Mappings, Research Report UCRL-MA-132239, Lawrence Livermore National Laboratory (1998).

[41] A. K. Kapila, D. W. Schwendeman, J. B. Bdzil, W. D. Henshaw, A study of detonation diffraction in the Ignition-and-Growth model, Combust. Theory and Modeling.